Turbulent spot formation in stably stratified three-dimensional Yukawa liquids

Suruj Kalita * and Rajaraman Ganesh
Institute for Plasma Research, HBNI, Bhat, Gandhinagar, Gujarat 382428, India
and Homi Bhabha National Institute, Training School Complex, Anushaktinagar, Mumbai 400094, India

(Received 22 August 2023; accepted 25 January 2024; published 23 February 2024)

A plane-Couette flow (PCF) is considered in a stably stratified three-dimensional (3D) Yukawa liquid, perturbed initially with a finite amplitude 3D perturbation. Stable stratification in density is achieved by subjecting the medium to external gravity. We demonstrate turbulent spot formation in a stably stratified PCF. The dynamics of the system is shown to depend upon the value of κ, which is associated with the range of interaction. We have performed "first principles" classical 3D molecular dynamics (MD) simulations for "hypergravity" ($1.3g_0$, g_0 is Earth's gravitational force for unit mass in our normalized unit) and "milligravity" ($9\times10^{-3}g_0$) cases for κ, 1.0 and 4.0, respectively. We extract relevant fluid quantities from MD data. For the hypergravity case, when the system is evolved in time under stable stratification, the kinetic energy is observed to deposit in the lower wave vectors (K_x, K_z), leading to "inverse cascade" in the plane perpendicular to the direction of stratification. As a result, we observe large-scale structure formation in velocity and streamwise vorticity fields. Nucleation of velocity streak is observed for the first time in the stably stratified case in our simulation. The coherent structures in the velocity and streamwise vorticity fields are found to sustain for longer period of time for the stably stratified cases as compared to the unstratified case. For the milligravity case, the large-scale dynamics is observed to enhance. Unlike unstratified PCF, a background flow in Y-averaged streamwise fluid velocity field is observed for the stably stratified case. We believe that our results using "first principles" classical MD simulations on subcritical turbulence in stably stratified Yukawa liquid, may have ramifications to wider class turbulence problems.

DOI: 10.1103/PhysRevResearch.6.013197

I. INTRODUCTION

Fluid turbulence, though deterministic, is not fully understood. A fluid becomes unstable, when its equilibrium is perturbed, provided that free energy is available to the system leading to instabilities, as a result of which, the system becomes turbulent with time. In a turbulent system, when energy is injected at a certain length scale or wave-vector value, the energy is transferred to a length scale smaller or larger than the energy injection length scale due to nonlinear coupling between modes. When energy transfers to smaller length scales as compared to the energy injection length scale, "forward energy cascade" ensues and when energy transfers to higher length scales, one observes "inverse energy cascade." For example, in three-dimensional (3D) homogeneous and isotropic turbulence, the forward energy cascade is known to occur, in which energy cascades towards the smaller length scales or to higher wave-vector values while in quasi-two-dimensional (2D) case, inverse energy cascade is observed, where energy cascades towards larger length scales or smaller wave-vector (K) values as compared to the injection length scale.

According to Kolmogorov theory given in 1941 for a 3D homogeneous and isotropic turbulence [1,2], the energy and helicity cascade in the forward direction (towards lower length scales or higher K) with a power law of $K^{-5/3}$. In the case of 2D turbulence, energy cascades in the reverse or inverse direction with a power law of $K^{-5/3}$ and enstrophy in the forward direction with a power law of K^{-3} [3]. In general, two forms of cascades are known to exist: dual cascade and split energy or bidirectional cascade. In dual cascade, two invariants, such as energy and enstrophy cascade in the opposite directions for 2D turbulence whereas, energy and helicity cascade in the same direction for 3D turbulence [4]. In split energy or bidirectional cascade, energy cascades in the forward and backward directions [5]. In Ref. [5], cascading of energy both in forward and backward directions in presence of rotation and stratification is demonstrated, which is observed in oceanic turbulence. It has been shown [6] that in general, flows in nature exhibit both 2D and 3D behavior. For example, Jupiter's and Earth's atmospheres exhibit both 2D and 3D behavior at different scale lengths. In Jupiter [7], at a length scale of 3500 to 40 000 KM (kilometer), enstrophy is observed to cascade in forward direction or downscale and the energy is observed to go upscale or in inverse direction. However, at a length scale lesser than 3500 KM, which is called the "deformation radius," the energy is observed to go downscale. In the case of Earth's atmosphere [4], energy mostly cascades

* suruj.kalita@ipr.res.in

in forward direction, but in the troposphere, at a length scale of 1000 to 5000 KM, energy and enstropy is observed to cascade in reverse and forward directions respectively. Earth and Jupiter's atmospheres set an example of both split energy and dual energy cascades, respectively. However, for inverse energy cascade to occur, two-dimensionality is not a necessary criterion. By changing the nature of the nonlinear terms in the Navier-Stokes equation, it was shown that energy cascades in the reverse direction with a power law of $K^{-5/3}$ and helicity cascades with a power law of $K^{-7/3}$ in the forward direction in 3D turbulence [8].

The cascade direction for transfer of energy depends upon various factors, such as, thickness of the fluid layer or confinement, rotation, stratification in density and, combined effect of rotation and stratification. In a fluid layer of finite thickness d (d is the vertical length of the fluid layer), the energy injection length scale l of the flow primarily controls the 3D and 2D behavior of the system. When $d > l$, the system behaves as a three-dimensional system. When $l > d$, the vertical wave number of the system, $K_{\rm v} = 2\pi/d$ becomes very large and the system effectively becomes two-dimensional (2D) or quasi-2D. In such quasi-2D system, the energy cascades towards larger length scales with a power law of $K^{-5/3}$ and the enstrophy, which is along the vertical direction, cascades in the forward direction with a power law of K^{-3}. In other words, by keeping l constant, when d is gradually reduced, at some particular thickness, split energy cascade is observed and further reducing the thickness, when the thickness reaches a critical value, unidirectional inverse cascade of energy is observed [9].

In the presence of a strong rotation as well, the system becomes quasi-2D, which can change the direction of energy cascade. In such rotation dominated system, the power law for inverse cascade is found to be K^{-2} [10] and K^{-3} [11], which is different from the conventional power law, $K^{-5/3}$, for inverse energy cascade in a quasi-2D system and forward energy cascade in a 3D isotropic and homogeneous turbulent system.

A stratification in density can also make a system quasi-2D by suppressing the motion along the stratification direction. In this context, in a stably stratified system, in which density reduces with the increase in height, a fully helical ABC flow have been investigated, at a high Froude number and moderate Reynolds number [12]. Due to the presence of stratification, large-scale structures are generated and, due to the combined effect of stratification and large-scale structures, helicity is found to decay slower than that of the unstratified case. Combining stable stratification with PCF, it was shown that fluid flow becomes more localized in space with an increase in stratification [13]. In forced stably stratified systems, forward cascade is observed in the past [14–17]. Detailed investigation of freely decaying stably stratified turbulence also have been studied in the past [18–20]. Various scale lengths associated with the stratified turbulence is discussed in Ref. [21]. Study of mixing efficiency using LES [22] and effect of eddy viscosity [23] is studied in details for stably stratified turbulence.

Presence of both rotation and stratification gives rise to "inverse cascade" in a system and create large-scale structures. In most of the planetary atmospheres, both rotation and stratification acts together and reverses the direction of energy flow at various length scales. The atmospheres of Earth, Jupiter, and Saturn are good examples of the combined effect of rotation and stratification [4,7]. The rate of an inverse cascade of energy depends upon the interplay between rotation and stratification, and when stratification dominates the rotation, the rate of inverse cascade of energy reduces [24].

In our present work, we have considered a stably stratified 3D Yukawa liquid in the presence of an external gravity. Using "first principles" classical 3D molecular dynamics (MD) simulation, we address the following questions: (1) starting from a PCF, is the formation of turbulent spot possible in a stably stratified 3D Yukawa liquid at all values of Reynolds number and in relatively small aspect ratio? (2) Is it possible to observe inverse cascade of kinetic energy and formation of large-scale structures in the presence of a stable stratification in a 3D Yukawa liquid, where the viscosity, ν and Reynolds number, Re is a function of time? (3) Does the stable stratification facilitate the coherent structures to survive for a longer period of time as compared to a unstratified case? (4) Does the range of interaction or the value of κ affect the turbulent dynamics of a stably stratified system? As our calculations are based on "first principles" classical MD simulation and as the "fluid" variables are constructed out of the instantaneous particle velocities and positions, our results are independent of the mathematical structure of conventional fluid dynamical systems such as Navier-Stokes equations.

Previously, many studies have been carried out in 2D Yukawa liquids, in the presence of an external gravity using MD simulation. For example, observation of Rayleigh-Bénard convection cells [25], observation of negative entropy production rate in a small subsystem of a 2D Yukawa liquid upto a finite observation time [26], transition from convective cells to shear/sheraless flow or zonal flow when a velocity perturbation [27] and, mass and charge inhomogeneity [28] is introduced to the system. In the above cases, density stratification was unstable in the presence of temperature gradient in the system. In contrast, we shall address the effect of stable density stratification in the spot formation process and cascade dynamics using fluid quantities extracted from MD data.

The rest of the paper is organized in the following way: In Sec. II, simulation details are given. In Sec. III, the results obtained from the MD simulation is discussed. In Sec. IV, we shall conclude and discuss our work.

II. SIMULATION DETAILS

To study the dynamics of turbulent spots in a stratified Yukawa liquid, we have upgraded an already reported 2D code [29] to MPMD-3D [30] with a "gravity module" incorporated in the solver. The MPMD-3D is parallelized in both CPUs and GPUs using MPI and open-ACC, respectively. Both versions of the code show good scaling with the increasing number of CPU cores or GPU cards. A schematic diagram of the system is shown in Fig. 1. The $\hat{x}$ and $\hat{z}$ directions are periodic while $\hat{y}$ direction is bounded. The dimension of the system along $\hat{x}$, $\hat{y}$, and $\hat{z}$ directions are $L_x = 493.77a$, $L_y = 50.02a$, and $L_z = 224.29a$. The equation of motion is normalized with "a"—the Wigner-Seitz radius for length scales and inverse of grain-plasma frequency, $\omega_{pd} = \sqrt{Q^2\bar{n}/\epsilon_0 ma^3}$ for timescales. Here, $\bar{n} = 3/4\pi$ is the normalized grain density, $m =$ mass of

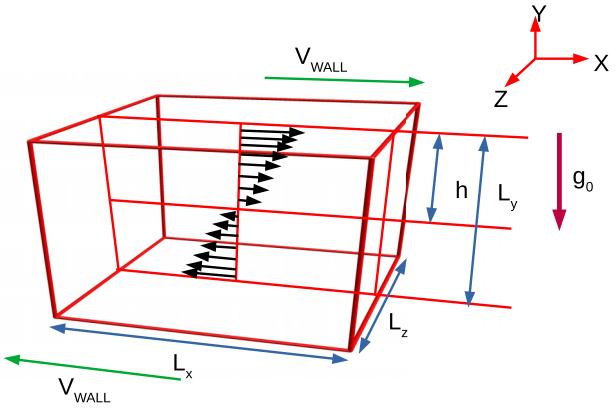

FIG. 1. In this schematic diagram, $\hat{x}$ and $\hat{z}$ directions are periodic while $\hat{y}$ direction is bounded. The system size is as follows: $L_x \times L_y \times L_z$ is $493.77 \times 50.02 \times 224.29$; $h = L_y/2$, is the half channel height. The external gravitational force on the system is acting along $-\hat{y}$ direction. The top and bottom walls translate opposite to each other with a velocity, $V_{\text{wall}} = 2.0$. As a result of the translation of the walls, a flow is generated in the system and the flow direction is shown by the arrows in the figure. When external gravity is nonzero, it induces stable stratification in density. This kind of flow is called—"plane Couette flow" (PCF) in a stratified medium. The streamwise, spanwise, and wall-normal directions are respectively $\hat{x}$, $\hat{z}$, and $\hat{y}$.

the grains, Q = charge of each grain. The aspect ratio of the system with respect to L_y, along $\hat{x}$ and $\hat{z}$ directions are $A_x = L_x/L_y = 9.87$ and $A_z = L_z/L_y = 4.48$. In this system, we have considered equal mass and charge for all the grains. The total energy (E) and temperature (T) of the system are normalized by $Q^2/4\pi\epsilon_0 a$. Consequently, the coupling strength Γ, which is the ratio of potential energy per grain to its kinetic energy, becomes $\Gamma = 1/\overline{T}$, where $\overline{T} = T/(Q^2/4\pi\epsilon_0 a)$ is the normalized grain temperature. The total potential energy in normalized unit is, $U_p(\vec{r}_i) = \sum_{j\neq i}^{N} exp(-\kappa r_{ij})/r_{ij} + \int_{-L_y}^{y_i} g dy$, N is the total number of grains. The first term represents the Yukawa interaction energy and the second term represents the potential energy due to the externally applied gravity. Thus the force on ith grain is

$$\vec{f}_i = \sum_{j\neq i}^{N} r_{ij}(1/(r_{ij})^3 + \kappa/(r_{ij})^2)\exp(-\kappa r_{ij})\hat{r}_{ij} - g\hat{y}. \quad (1)$$

The above Eq. (1) is a normalized equation. Here, $\kappa = r/\lambda_D$ and λ_D is the screening length, which, for example, is governed by background ion temperature in a complex plasma [30,31]. As, $\kappa = r/\lambda_D$, lesser value of κ stands for weak shielding of the charge and the range of interaction is relatively higher as compared to higher value of κ.

To begin with the simulations, a Gaussian thermostat is used to thermalize the grains at a desired temperature, based on the "Gaussian principle of least constraint" [32]. After thermalizing the grains at a desired temperature, the grains are subjected to an external gravity in two steps [26,33]. The gravitational force is applied along $-\hat{y}$ direction. The grains are equilibrated under the gravitational force in two steps. In the first step, the grains are evolved under external gravity with a Gaussian thermostat upto 15 000 ω_{pd}^{-1} and in the second step, from 15 001 ω_{pd}^{-1} to 20 000 ω_{pd}^{-1}, the grains are evolved microcanonically, without any thermostat. In a typical laboratory conditions, the grain plasma frequency (ω_{pd}) is of the order of 10–100 Hz [34] and the Wigner-Seitz radius (a) is around 0.40–0.58 mm [35]. Hence, the external gravity or the earth's gravity in the normalized unit is, $g_0 = g/a\omega_{pd}^2 = 0.063$. For a given value of κ, which decides the range of interaction between grains, the value of "g" is chosen in such a way that the external gravitational force roughly balances interparticle interaction force. A stronger gravity (higher value of "g") will result in a compression of the liquid, near the bottom plate and a feeble gravity (smaller value of "g") will produce weak stratification in the density of the system. Here, the value of "g" is chosen in such a way that for a given value of κ, a stable stratification in density is achieved as well as there is minimal compression of the fluid. In this work, we have used two values of κ, viz. $\kappa = 1$ and $\kappa = 4$, as used in our previous work [30]. The range of interaction for $\kappa = 4.0$ is less as compared to $\kappa = 1.0$. Hence, the Yukawa liquid at $\kappa = 4.0$ is easy to compress as compared to $\kappa = 1.0$. Therefore, to produce a stable density stratification, a smaller value of $g = 0.009g_0$ is chosen for $\kappa = 4.0$ and a relatively higher value of $g = 1.3g_0$ is chosen for $\kappa = 1.0$.

After obtaining a stably stratified fluid at a desired average grain temperature; $\overline{T} = 0.00067$ ($\Gamma = 1500$) for $\kappa = 1.0, 4.0$; a plane Couette flow (PCF) is superposed on each thermalized grain as follows: $\mathrm{v}_{xi} = \mathrm{v}_{xi} + 2V_{\text{wall}}/L_y$; $V_{\text{wall}} = 2.0$; is the top and bottom wall speed. As the both top and bottom walls move with equal and opposite velocities (Fig. 1), the fluid in between the two moving walls attains a linear velocity profile. The details of imposing a PCF at the initial time is described in Ref. [30].

The characteristic velocity profile for PCF is linearly stable at all the values of Reynolds number (Re) [36]. To investigate the turbulent dynamics of PCF, the flow must be subjected to a finite amplitude, three-dimensional (3D), nonlinear perturbation. However, the turbulent dynamics of such flows also depend upon the aspect ratio of the system, where, for example, a 3D nonlinear or noisy initial perturbations generate turbulent structures (turbulent spots or streaks, turbulent bands) [37–39]. However, both kinds of initial perturbations mentioned above make the flow turbulent [39,40]. To study the turbulent dynamics of PCF in a stably stratified 3D Yukawa liquid, we consider Lundbladh-like [39] 3D nonlinear perturbation. The form of perturbation is given as follows:

$$\mathrm{v}_{yi}^{\text{pert}} = \mathrm{y}_i\left(h^2 - \mathrm{y}_i^2\right)^2 \frac{x_i}{\delta_x} e^{-\left[\left(\frac{x_i}{\delta_x}\right)^2 + \left(\frac{z_i}{\delta_z}\right)^2\right]} \frac{1}{\delta_z}\left(1 - 2\left(\frac{z_i}{\delta_z}\right)\right)^2, \quad (2)$$

$$\mathrm{v}_{zi}^{\text{pert}} = -\left(\frac{x_i}{\delta_x}\right)\left(\frac{z_i}{\delta_z}\right)\left(h^2 - \mathrm{y}_i^2\right) e^{-\left[\left(\frac{x_i}{\delta_x}\right)^2 + \left(\frac{z_i}{\delta_z}\right)^2\right]}\left(h^2 - 5\mathrm{y}_i^2\right). \quad (3)$$

The perturbations applied at the particle level on the ith grain is given as follows:

$$\mathrm{v}_{yi} = \mathrm{v}_{yi} + A\mathrm{v}_{yi}^{\text{pert}}, \quad (4)$$

$$\mathrm{v}_{zi} = \mathrm{v}_{zi} + A\mathrm{v}_{zi}^{\text{pert}}. \quad (5)$$

Here, there is no perturbation along the streamwise direction velocity (v_{xi}). In the above equations, the perturbations are applied to the particles, which are in the range $-30a \leqslant x \leqslant 30a$ and $-30a \leqslant z \leqslant 30a$. In Eq. (2), $\delta_x = \delta_z = 12a$, is the fall-distance of the applied perturbations along $\hat{x}$ and $\hat{z}$ directions. The perturbation strength A is chosen in such a way that the maximum fluid V_y does not exceed 75 % of the V_{wall}. More details regarding the perturbations is given in Ref. [30].

As our simulations are at the particle level, we have all the information at the particle level. To construct the fluid variables or the macroscopic quantities from the instantaneous particle level data obtained from our 3D classical MD simulations, we implement the method of "fluidization" [30,41]. An Eulerian grid in 3D having 3D cells along $\hat{x}$, $\hat{y}$, $\hat{z}$ is N_x, N_z, N_z, such that $N_x \times N_y \times N_z$ is $46 \times 19 \times 28$, which is superimposed onto the system containing the particles. Total number of particles in the system is 1.318554×10^6 and after fluidization, particles per 3D cell is around 53. We find that this many number of particles per cell is sufficient to capture the essential fluid characteristics of the system. All the results presented below are given in-terms of the fluid variables.

We have demonstrated earlier [30] that a PCF becomes unstable when perturbed with a finite amplitude 3D nonlinear perturbation, which leads to turbulence via spot formation in a very small aspect ratio system ($A_x \approx 10$), when the applied perturbation amplitude is above a critical value. This class of turbulence is shown to be subcritical [30,42]. In addition to this, we have demonstrated that the results tend to be more fluid like, when the range of interaction is increased, or the value of κ is decreased from 4.0 to 1.0 [30]. We found that for smaller range of interaction ($\kappa = 4.0$), the system is dominated by large-scale flow while for larger range of interaction ($\kappa = 1.0$), the system is dominated by both large and small scales. However, at late times, the dynamics is largely dominated by small scales. Figure 16 in Ref. [30] shows the spot formation for two different κ values. For $\kappa = 1.0$, the V_x fluid velocity field is filled with velocity streaks surrounded by large-scale structures or flow while for $\kappa = 4.0$, we observe only large-scale flow.

In our present work, we have incorporated an external gravity in the system to study the spot formation dynamics in a stratified environment. As an initial condition, we have perturbed the system as shown in Eqs. (4) and (5). As a boundary condition, we have implemented "moving wall boundary condition" to translate the top and bottom walls opposite to each other and the details of its implementation is given in Ref. [30]. Using "first principles" classical MD simulation, we solve Eq. (1), with initial and boundary condition mentioned above. For all the numerical experiments, we have used $g = 1.3g_0$ for $\kappa = 1.0$ and $g = 0.009g_0$ for $\kappa = 4.0$.

III. RESULTS

After preparing the initial state for different cases, we evolve the initial state using the MPMD-3D [29,30]. For the gravitated case we simply turn on the gravity module embedded into the code. After the perturbation is added, the system is evolved up to 250 or 300 ω_{pd}^{-1}, we analyze the results and the results are presented below.

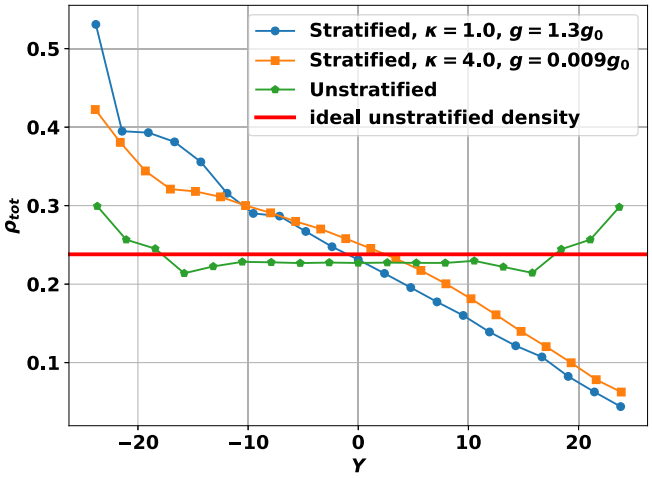

FIG. 2. The density (ρ_{tot}) of the system as a function of "Y" is shown. According to the "a" normalization, the ideal unstratified density is $3/4\pi$ or 0.238. The computed density for the unstratified case is nearby 0.238, except few deviations near the wall location. For the stratified and $\kappa = 1.0$ case, the density near the top wall is 0.043 and near the bottom wall is 0.64. For the $\kappa = 4.0$ case, density near the top wall is 0.063 and near the bottom wall is 0.45. The variation in density for both the cases is found to be around the base density, 0.238. A nearly linear variation of density is observed for both the stratified cases. This near linear variation of density is playing a key role in controlling the dynamics of the gravitated system.

A. Results for $\kappa = 1.0$

We shall first discuss the results for $\kappa = 1.0$ with stratified and unstratified cases. The instantaneous density profile for the stratified and unstratified cases at $t = 0$ is shown in Fig. 2 After averaging over the $\hat{x}$ and $\hat{z}$ directions, as a function of Y. It is to be noted that the instantaneous density profile for stratified case is not exactly a straight line and for unstratified case, the instantaneous density profile is not a straight line with zero slope. There are some nonuniformities at the boundary along $-\hat{y}$ direction for the stratified case. The reason for having such nonuniformity at the boundary is because we have "free reflective boundary condition" in the $\hat{y}$ direction and the external gravity acts in the $-\hat{y}$ direction, due to which slightly more number of particles gather at the boundary along $-\hat{y}$ direction. Despite having such nonuniformity in the density profile at y boundaries, our simulation is able to bring out the important effects that arise due to the presence of stable density stratification in a system.

1. Fluid velocity

Figures 3–6 show the fluid V_x, V_y velocities [43–47] for the stratified case at $\kappa = 1.0$. In Fig. 3, a spot structure for the stratified case in V_x velocity fields is observed, which elongates in space ($\hat{x}$, $\hat{z}$ directions) with time. We observe three velocity streak formations in the system. Velocity streaks are regarded as small scale structures in a turbulent spot and surrounding the velocity streaks, large-scale flow structure from 65 to 85 ω_{pd}^{-1} is observed. There is a continuous growth in the size of the velocity streaks with time along $\hat{x}$ and $\hat{z}$ directions. At time 235 to 250 ω_{pd}^{-1}, the central velocity streak

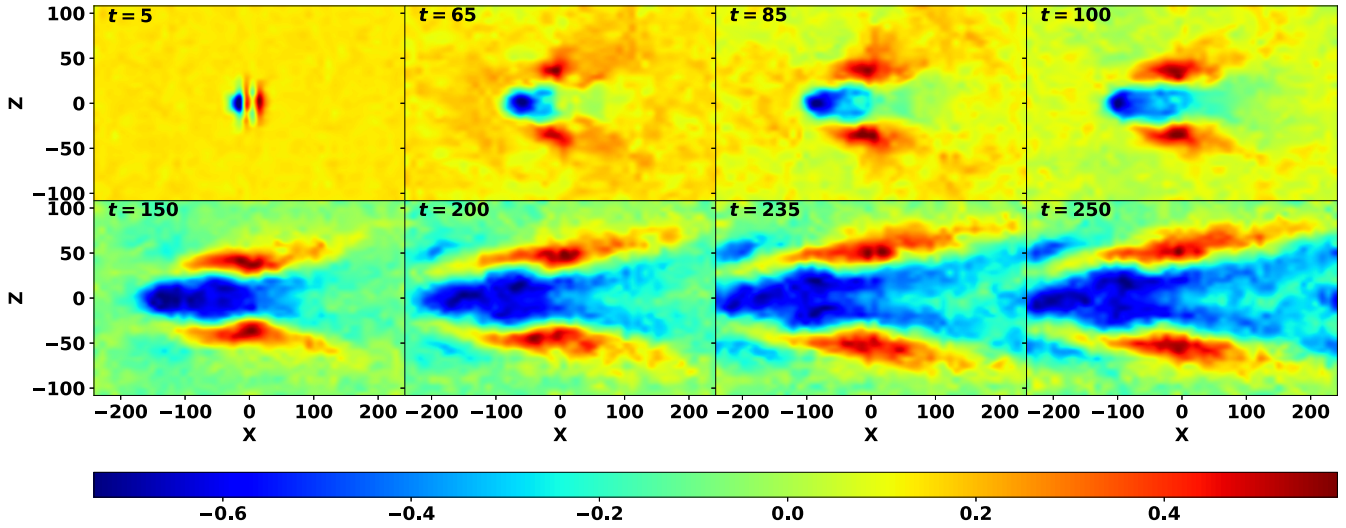

FIG. 3. Time evolution of the streamwise fluid velocity V_x for the stratified case in $Y = 0$ plane as a function of X and Z is shown. At time $t = 65$, 85 ω_{pd}^{-1}, we observe large-scale flow surrounding the turbulent streaks. We observe three velocity streaks for this case. The velocity streaks grow in size continuously and after 150 ω_{pd}^{-1}, the central velocity streak is observed to fill the entire X region around $Z = 0$.

is observed to re-appear in the positive $\hat{x}$ direction in the XZ plane at $Y = 0$ due to periodic boundaries.

We compare our stratified results shown in Fig. 3 to the results obtained for the unstratified case for identical parameters and the comparison is shown in Fig. 4. In Fig. 4, fully developed velocity streaks at around $t = 45 - 50\ \omega_{pd}^{-1}$ for the unstratified case are observed while for the stratified case the streaks generate at late times and becomes well-defined from $t = 85$–$90\ \omega_{pd}^{-1}$. In the presence of stratification, the symmetry along $\hat{x}$ direction of the velocity streaks is broken, as the streaks have shifted more towards left from $t = 45$ to 120 ω_{pd}^{-1}. An increase in the length scale is obvious for the stratified case, as the number of velocity streaks have reduced to 3, from 5, as shown in unstratified case. Overall, the spatial spread of the velocity streaks for the stratified case has increased significantly as compared to the unstratified case. More details regarding the spatial spread of the spot is discussed in "Spatiotemporal Analysis" section.

Let us now consider the V_y fluid velocity field as shown in Fig. 5 in $Y = 0$ plane as a function of X and Z. At the initial time ($t = 10$), the spot structure is symmetric along $\hat{x}$ and $\hat{z}$ directions. As the time evolves, the spot structure moves more towards the $-\hat{x}$ direction. The velocity streaks start to generate or develop at $t = 60\ \omega_{pd}^{-1}$ and becomes well-defined at $t = 95\ \omega_{pd}^{-1}$. At this time, three velocity streaks (two negative and one positive) are observed. With further evolution in

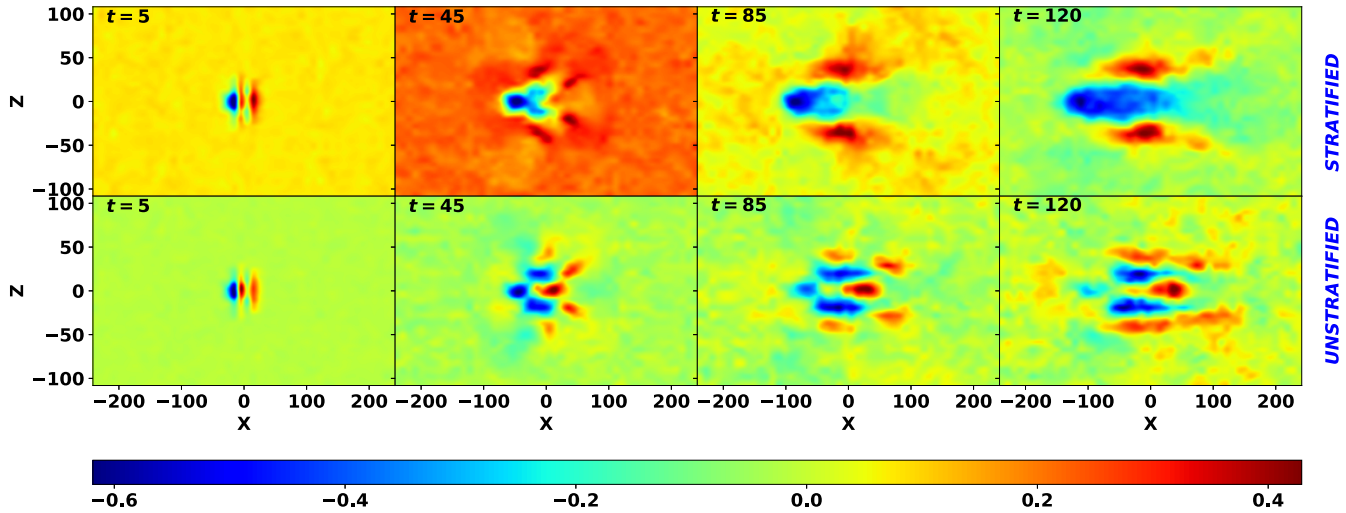

FIG. 4. Comparison of streamwise fluid V_x velocity between the stratified and unstratified cases at $Y = 0$ plane as a function of XZ is shown. At $t = 5\ \omega_{pd}^{-1}$, the spot structures look similar. After that, streaks start to develop for both the cases. At $t = 85\ \omega_{pd}^{-1}$, three velocity streaks are observed for the stratified case and for the unstratified case, numerous such streaks are observed, which end up having five well-defined velocity streaks at $t = 120\ \omega_{pd}^{-1}$, which remains stable with further evolution of time. The reduction in the number of velocity streaks from 5 to 3 at the same location at $t = 120\ \omega_{pd}^{-1}$, implies the dominance of large-scale flow in the system for the stratified case.

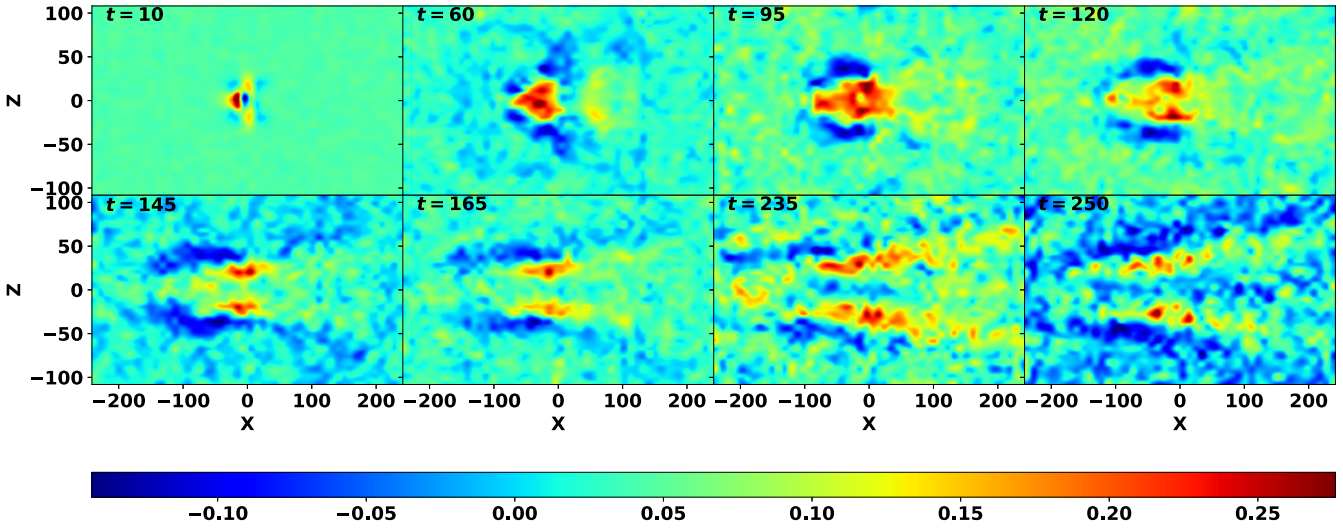

FIG. 5. Time evolution of the wall-normal fluid velocity V_y at $Y = 0$, as a function of XZ is shown. The spot structure appears at $t = 10\ \omega_{pd}^{-1}$. From $t = 60\ \omega_{pd}^{-1}$, the velocity streaks start to develop, and at $t = 95\ \omega_{pd}^{-1}$, we observe three velocity streaks. The splitting and generation of streaks is observed from $t = 120$ to $250\ \omega_{pd}^{-1}$. As the streaks tend to cover the entire simulation domain, a large-scale flow is dominant in the system.

time, the central positive velocity streak splits into two segments at time, $t = 120$–$130\ \omega_{pd}^{-1}$. At time, $t = 150\ \omega_{pd}^{-1}$, a new negative velocity streak of very small magnitude is nucleated in between the two positive velocity streaks that split earlier. From 165 to $250\ \omega_{pd}^{-1}$, we observe five velocity streaks in V_y fluid velocity field, three negative and two positive. It is to be noted that the central negative velocity streak nucleated at around 145–150 ω_{pd}^{-1} have very small magnitude, but at later times the magnitude of the central velocity streak increases and becomes visible clearly from 235 ω_{pd}^{-1}. In addition to this, the velocity streaks tend to cover the entire simulation domain (XZ plane at $Y = 0$) up to $250\ \omega_{pd}^{-1}$ (maximum simulation time). There is a generation of small-scale structure in V_y velocity field. However, the velocity streaks continue to extend in space with time. Hence, the system is dominated by large-scale dynamics, suppressing the small-scale ones.

We compare the V_y fluid velocity fields for the stratified case with that of the unstratified case, which is shown in Fig. 6. At the initial time, $t = 10\ \omega_{pd}^{-1}$, both the spot structures are symmetric along $\hat{x}$ and $\hat{z}$ directions. In both cases, the velocity streaks evolve in the same timescale. However, the width of the velocity streaks for the stratified case is larger as compared to the unstratified case. At $t = 105\ \omega_{pd}^{-1}$, three velocity streaks are observed for the stratified case and five velocity streaks for the unstratified case (three negative, two positive). As the time evolves, the spot structure in V_y velocity fields for the unstratified case ceases to exist after $150\ \omega_{pd}^{-1}$ due to increased heating in the system [30,41]. On the other hand,

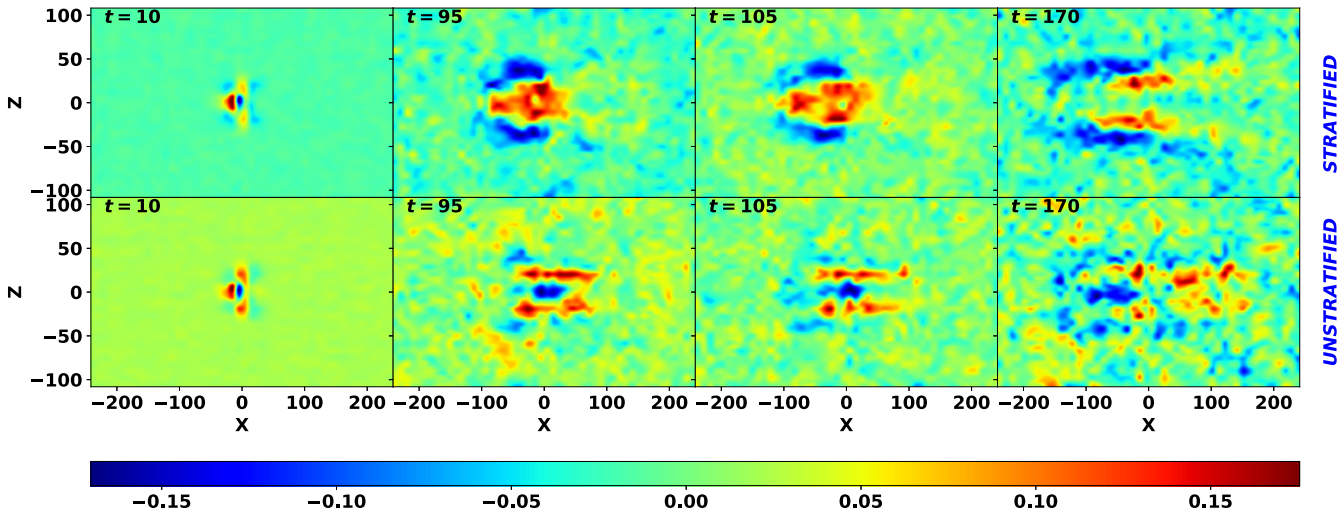

FIG. 6. Comparison of the wall-normal fluid velocity V_y for the stratified and unstratified cases at $Y = 0$ plane, as a function of XZ is shown. At the initial time, the spot structure looks similar for both cases. Here also, we get five velocity streaks for the unstratified case and three for the stratified case, which later becomes 5. Looking at $t = 170\ \omega_{pd}^{-1}$, we can say that the structures retain for a longer period of time for the stratified case.

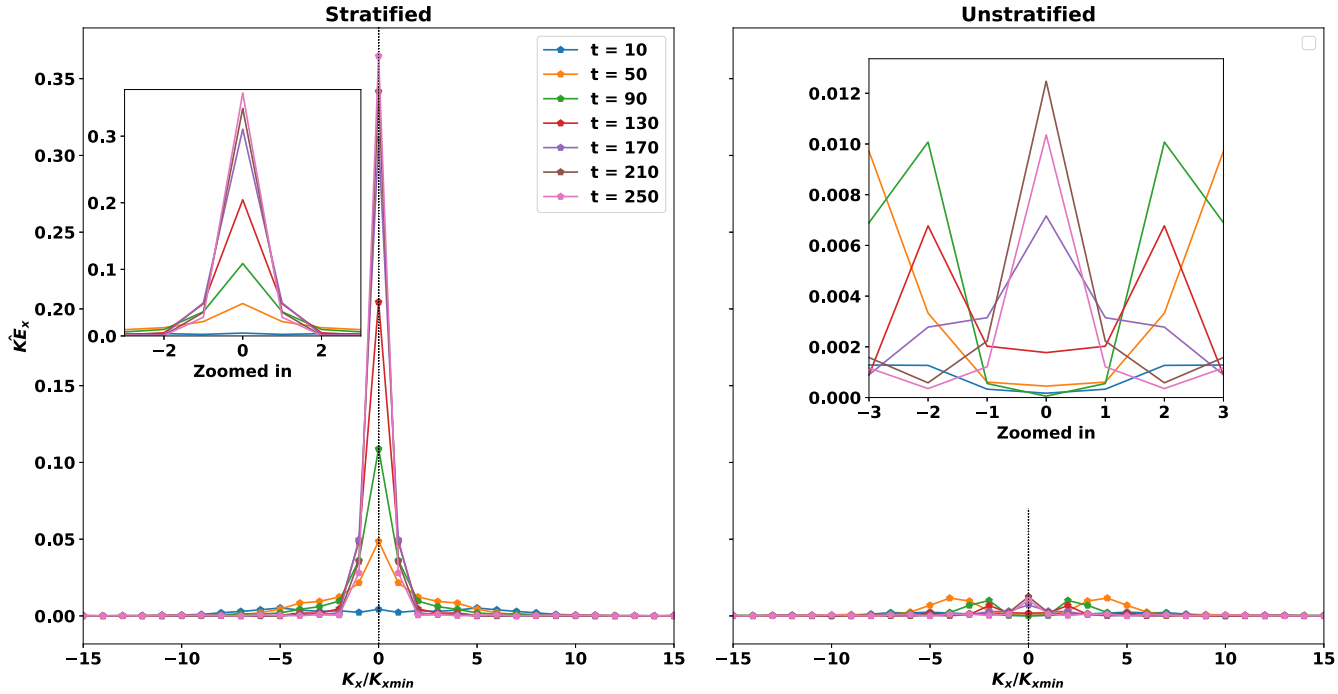

FIG. 7. One-dimensional Fourier transform of X kinetic energy in the mid YZ plane ($\hat{KE}_x$) as a function of $K_x/K_{x_{\min}}$ is shown. For the stratified case, the energy continuously deposits into the lower $K_x/K_{x_{\min}}$ values. Therefore the energy at the lowest $K_x/K_{x_{\min}}$ increases with time. For the unstratified case, the energy at the lowest $K_x/K_{x_{\min}}$ increases up to 50 ω_{pd}^{-1}. Then, over time, it gets smaller and becomes equal to the energy, which was at $t = 10\ \omega_{pd}^{-1}$. This is consistent with the fact that the dynamics of the system is governed by the small-scale structures at later times.

new velocity streaks are nucleated for the stratified case and at the end of the simulation we observe five velocity streaks. One important point to be noted here is that the spot structure survives for a longer period of time for the stratified case, as compared to the unstratified case, despite having the same initial perturbation strength. Moreover, the velocity streaks for both V_x and V_y velocity fields are found to be oblique with respect to the streamwise direction ($\hat{x}$) [37,38,44]. The V_y velocity contours shown in Figs. 5 and 6 are not very well-defined as the V_x velocity contours, as there is no zeroth-order flow along $\hat{y}$ direction [30].

The size of the spot structure in both velocity fields (V_x, V_y) observed to increase spatially with time; we therefore perform a Fourier analysis of the velocity fields to identify whether there is any dominant large-scale mode present in the system. As the velocity streaks for V_x are more well-defined as compared to V_y velocity streaks. Therefore we shall analyze the V_x velocity field in the Fourier space.

2. Analysis in Fourier space

At first, we perform the one-dimensional Fourier transform (1d FFT) of the fluid X kinetic energy, $KE = 0.5 * V_x^2$, in the mid plane $Y = 0$ as a function of X ($Z = 0$) and Z ($X = 0$). The Fourier transform of KE is determined by constructing $0.5(\hat{V}_x.\hat{V}_x^*)$. Here, $*$ denotes complex conjugate and $\hat{}$ represents Fourier transform. Figures 7 and 8 show the Fourier transform of KE in the mid YZ and XY plane, as a function of $K_x/K_{x_{\min}}$ and $K_z/K_{z_{\min}}$. Also $K_{x_{\min}} = 2\pi/L_x$, $K_{z_{\min}} = 2\pi/L_z$. Therefore $K_x = K_{x_{\min}}(n_x - 1)$, $nx <= N_x/2$; $K_{x_{\min}}(-n_x + N_x + 1)$, $nx > N_x/2$. The definition of K_z is the same as K_x.

Let us consider the plot of 1d Fourier transform of the X kinetic energy, $\hat{KE}_x$ versus $K_x/K_{x_{\min}}$ in Fig. 7. We observe that the energy gets continuously deposited into decreasing $K_x/K_{x_{\min}}$ values. At $t = 10$, the energy at the smaller $K_x/K_{x_{\min}}(\simeq 0.0)$ is around 0.004301; with the evolution of time, there is an increase in the energy stored at the lowest $K_x/K_{x_{\min}}$ value and at the end of the simulation, at $t = 250\ \omega_{pd}^{-1}$, the peak value is 0.364808. There is an increase of 8381.93% or 84.81 times in the value of $\hat{KE}_x$ at $t = 250\omega_{pd}^{-1}$ from $t = 10\omega_{pd}^{-1}$. From the time evolution of the $\hat{KE}_x(k_x)$ graph, it is clear that energy at the higher value of wave vectors decreases while the energy at the smaller wave vectors increases with time. After comparing the stratified results with that of the unstratified one (Fig. 7), we find that for the unstratified case, the energy grows at the smallest K_x value up to $t = 50\ \omega_{pd}^{-1}$. After $t = 50\ \omega_{pd}^{-1}$, the energy decreases up to $t = 130\ \omega_{pd}^{-1}$ and become nearly equal to the energy, which was at $t = 10\ \omega_{pd}^{-1}$. It is already well known from our previous work that for unstratified case at $\kappa = 1.0$, the system is both governed by large and small scales [30]. At later times, the large-scale flow amplitude decreases and small-scale flow amplitude increases.

In Fig. 8, we consider the 1d Fourier transform of the X kinetic energy, $\hat{KE}_z$ versus $K_z/K_{z_{\min}}$. The general trend of energy deposition at the lower wave vectors is not the same

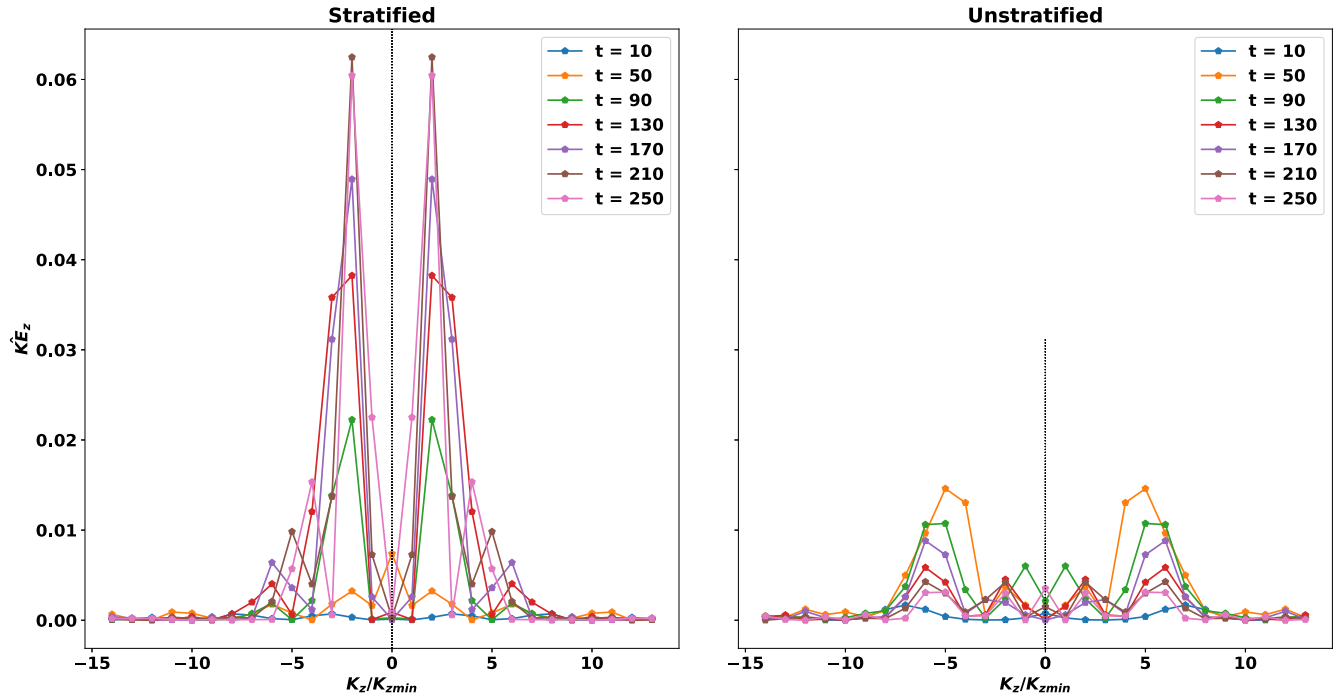

FIG. 8. The variation of one-dimensional Fourier transform of X kinetic energy in the mid XY plane ($\hat{KE}_z$) as a function of K_z is shown. For the unstratified case, energy continuously deposits into the $K_z/K_{z_{\min}} > 5$ or 6, up to $t = 50\ \omega_{pd}^{-1}$ and then it starts to fall over time. This is also consistent with the fact that the system later governed mostly by the small-scale dynamics.

as that of the earlier case, as shown in Fig. 7. Here, the energy is observed to deposit continuously in $K_z/K_{z_{\min}} = 2$. At $t = 10\omega_{pd}^{-1}$, the energy at $K_z/K_{z_{\min}} = 2$ is 0.000323 for the stratified case and at $t = 250\omega_{pd}^{-1}$ it becomes 0.060447. So, the energy increases by 18614.24% or 187.14 times for the stratified case. However, the energy tends to decrease from $t = 210\omega_{pd}^{-1}$, as there is no zeroth-order flow along $\hat{z}$ direction. On the other hand, for the unstratified case, the energy increases up-to time $t = 50\omega_{pd}^{-1}$ at $K_z/K_{z_{\min}} > 5$ or 6 and then decays with time. The modal distribution of energy indicates the fluid becoming homogeneous or laminar with time. From Figs. 7 and 8, we observe that energy is increasing in the lower modes($K_x/K_{x_{\min}} = 0, K_z/K_{z_{\min}} = 2$, respectively), which in accordance with the formation of large-scale structures shown in Figs. 3 and 4, where the spot structure starting from a very small in size, grows in size and almost occupies the entire space in XZ plane with time. We call this event as the occurrence of "inverse cascade" in the system.

Apart from the 1d FFT diagnostics of kinetic energy, we have constructed the two-dimensional (2D) scale-weighted power spectra or Pre-multiplied power spectra [30,48,49] at $Y = 0$ plane as a function of X and Z. More details can be found in Ref. [30]. This is an interesting diagnostics that determines whether there is only large-scale flow or both large and small scale flows present in the system. The construction of the 2D premultiplied power spectra is obtained by multiplying the wave vector $K = \sqrt{(K_x)^2 + (K_z)^2}$ with the 2D Fourier transform of X or Z kinetic energies. Here, $K\hat{E}_x$ and $K\hat{E}_z$ are the instantaneous premultiplied power spectra for X and Z kinetic energies. In $K\hat{E}_{x/z}$, K is the wave vector mentioned above and $\hat{E}_{x/z}$ is $|\hat{V}_{x/z}|^2$, where $\hat{V}_{x/z}$ is the 2D fourier transform of $V_{x/z}(X, Z)$. The Fourier transformed quantity $\hat{E}_{x/z}$ is calculated in the same way as we calculated $\hat{KE}$ above.

Figure 9 shows the instantaneous $K\hat{E}_x$ for stratified and unstratified cases. From our previous work [30] one finds that for unstratified case we have both large and small scales present in the system. With time, both large and small scale amplitudes rise from $t = 50$ to $100\ \omega_{pd}^{-1}$ (at $\lambda/h = 6.16$, 1.47 respectively). However, as time evolves, the large-scale flow amplitude tends to decrease with time from $t = 100$ to $150\ \omega_{pd}^{-1}$ while the small-scale flow amplitude increases from $t = 100$ to $150\ \omega_{pd}^{-1}$. Hence, one can surmise that both large and small scales are present in the system. At later times, small-scale dynamics dominate over the large-scale dynamics in the unstratified case. For the stratified case, the energy at the higher wavelength is greater than that at the shorter wavelengths. The energy at the higher wavelength ($\lambda/h = 4.133$) is observed to increase from the order of 10^1 to above the order of 10^2 (in the logarithmic scale), at times, $t = 50$ to $150\ \omega_{pd}^{-1}$. Therefore dynamics of the stratified case is largely governed by the large-scale flow dynamics.

We further consider the time averaged plot of the Pre-multiplied power spectra along $\hat{x}$, which is $\langle K\hat{E}_x \rangle$ [30,49]. The averaging is performed from 80 to 125 ω_{pd}^{-1}, over nine samples, when the turbulent spot becomes well-defined. The time averaged Pre-multiplied power spectra $\langle K\hat{E}_x \rangle$ is shown in Fig. 10. For the unstratified case, we observe two distinct peaks for large and small scale flow. The large-scale flow peaks at $\lambda_m/h = 6.1620$ and small-scale follow peaks at $\lambda_m/h = 1.4710$. Here, λ_m corresponds to the two distinct peaks. We now calculate the large and small scale flow amplitude by the following formula, $A_x^{lsf} = \langle K\hat{E}_x \rangle(\lambda = \lambda_m)/V_{\text{wall}}^2$

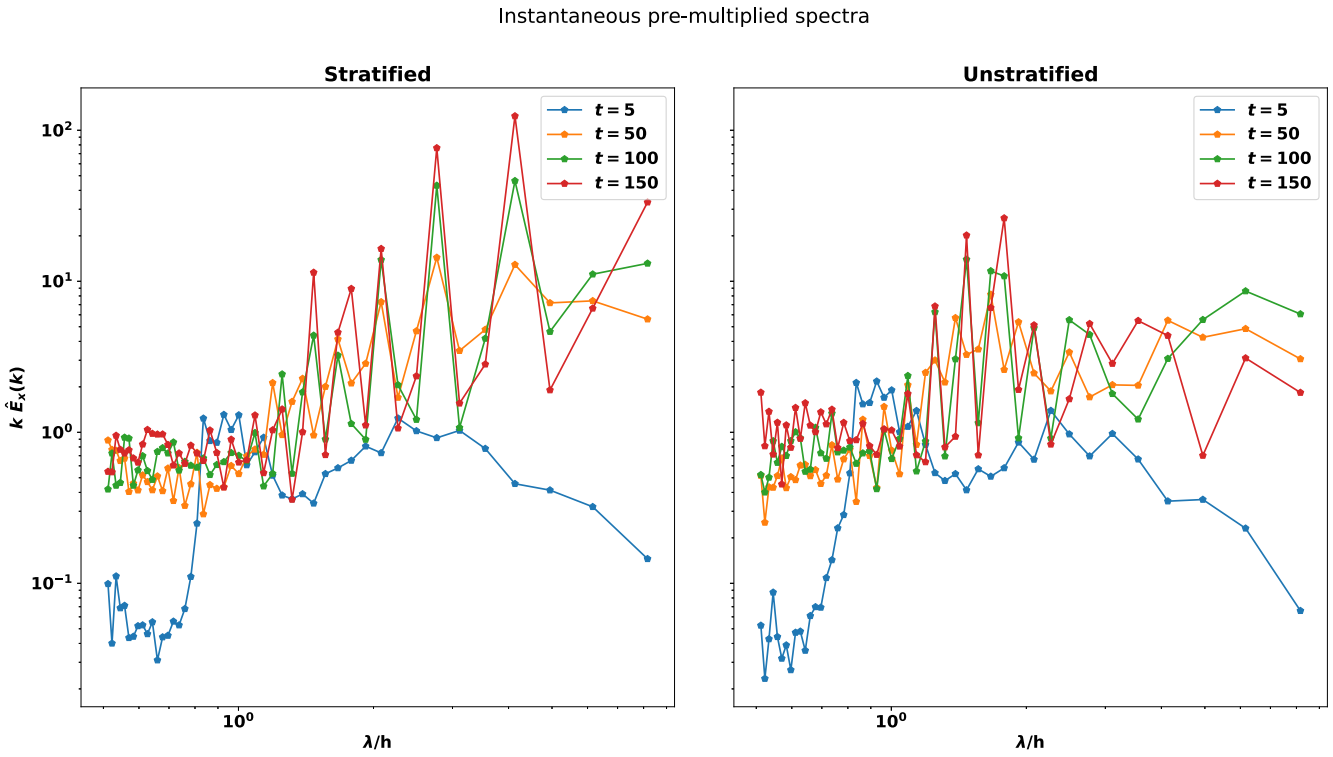

FIG. 9. Instantaneous scale-weighted or premultiplied power spectra ($K\hat{E}_x$) at $Y = 0$ plane, as a function of $\lambda = 2\pi/K$ is shown. For the stratified case, The spectral energy increases with time at the higher values of λ. This implies the dominance of large-scale flow in the system. For the unstratified case, there is a scale separation in the system, which implies that there is a presence of both large and small scales in the system.

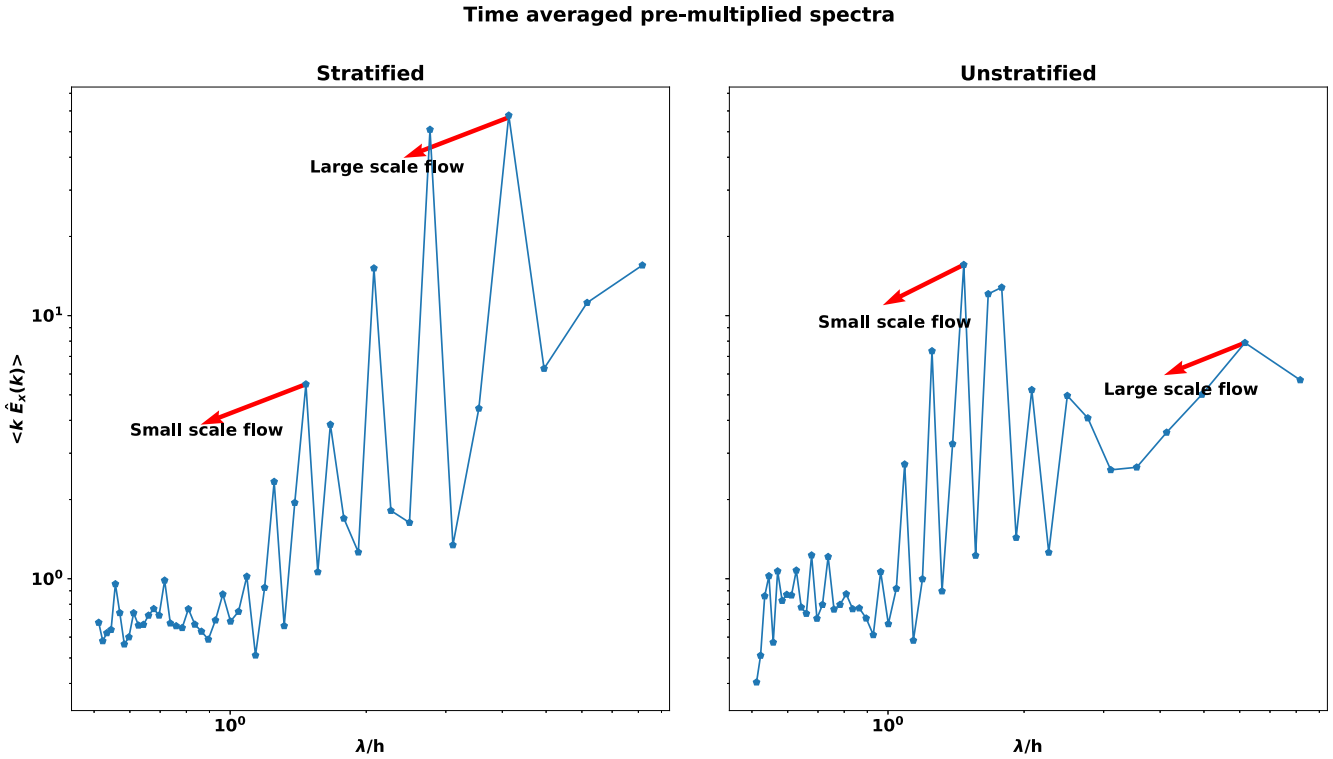

FIG. 10. Time averaged scale-weighted or premultiplied power spectra for the stratified and unstratified case is shown. In order to explain the diagram better, we have indicated the dominant "Large" and "Small" scale flow ($\lambda = \lambda_m$) values to be 4.13390h, 1.4710h and 6.1620h, 1.4710h for the stratified and unstratified cases respectively.

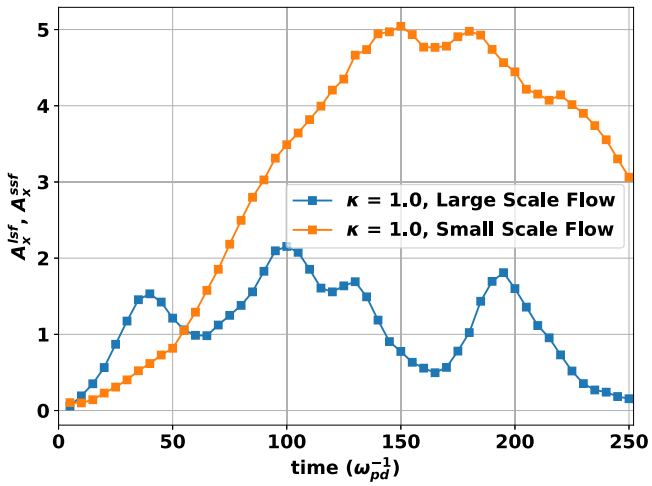

(a) Unstratified case.

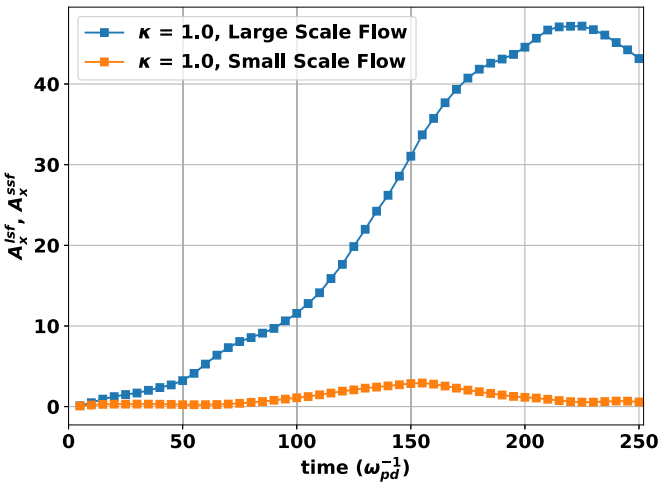

(b) Stratified case.

FIG. 11. In (a) and (b), we have shown the large-scale (A_x^{lsf}) and small-scale flow amplitude (A_x^{ssf}) for the unstratified and stratified cases respectively. For the unstratified case, the A_x^{lsf} takes a moderate value while for the stratified case, the value of A_x^{lsf} increases monotonically with time. (a) Unstratified case. (b) Stratified case.

and $A_x^{ssf} = \langle K\hat{E}_x \rangle(\lambda = \lambda_m)/V_{\text{wall}}^2$. For the stratified case, the large-scale flow peaks at $\lambda_m/h = 4.1339$. It is challenging task to determine the dominant wavelength for the small-scale flow, as the system is mostly dominated by large-scale flow. However, taking analogy from the unstratified case, let us consider the dominant wavelength (λ_m) for the small-scale flow to be $1.4710h$. The comparison between the small-scale flow (A_x^{ssf}) and large-scale flow amplitude (A_x^{lsf}) for stratified and unstratified cases are shown in Fig. 11 and it shows that A_x^{lsf} decreases and A_x^{ssf} increases with time for the unstratified case. On the other hand, for the stratified case the A_x^{lsf} increases significantly with time as compared to A_x^{ssf}. The results shown in Fig. 11, is consistent with the earlier diagnostics, which shows that the small-scale flow dominates over the large-scale flow for the unstratified case at later times while for the stratified case, the large-scale flow overwhelmingly dominates over the small scale flow in the system. Again, comparing the magnitude of A_x^{lsf} for the stratified and unstratified cases from Fig. 11, we find that the large-scale flow is highly dominant for the stratified case. The maximum value of A_x^{lsf} for the unstratified case is just 4.44% of the maximum A_x^{lsf}, for the stratified case.

From the above analysis, it is clearly observed that the large-scale flow dominates over the small scale-flow for the stratified case. Consequently, there is an up-scale energy transfer in the system, provided there is a density stratification due to an external gravity. Hence, there is an "inverse cascade" in the system, which generates large-scale structures in the stratified system at lower value of κ, which is 1.0. To know more about the growth of the spot structure or level of intermittency in the system, we investigate the spatiotemporal properties of the system.

3. *Spatiotemporal analysis*

The spatiotemporal diagram for the stratified and unstratified case is shown in Fig. 12. The plot is shown in mid X plane, at $Y = 0$ and we have shown the fluid V_x velocity as a function of Z and t. More details regarding construction of spatiotemporal plot can be found in Ref. [30]. For the unstratified case, we find that the spot structure spreads spatially very quickly at around 5 ω_{pd}^{-1}. However, at later times the spread almost becomes zero. As, the large-scale flow amplitude decreases with time and the system is mostly dominated by the small-scale flow. For the stratified case, the spread of the turbulent spot looks similar to the unstratified case up to 50 ω_{pd}^{-1}. However, after 50 ω_{pd}^{-1}, the turbulent spot structure tends to spread though out the entire Z locations. The datum corresponding to tracking the edge of the turbulent spot as shown in the Fig. 12 and the tracked boundary is shown in Fig. 13. From Fig. 13, we find that the spread for the stratified case is higher as compared to the unstratified case. Therefore one may surmise that the intermittency for the stratified case has increased due to the presence of the density stratification created by the external gravity. The number of streaks observed for the unstratified case is large as compared to the stratified case. In both the cases the number streaks remain constant. No new streaks found to nucleate for V_x velocity fields as a function of time. From this diagnostics, it is very clear that the length scale for the stratified case has increased. Therefore large-scale flow is dominant in the system and the spot structure continuous to grow with time for the stratified case.

Apart from the spatiotemporal diagram, another method to determine the intermittency or anisotropy in the system is to construct probability distribution function (PDF) of velocity fields or their gradients. Following Ref. [21], we have constructed the PDF of $\partial V_y/\partial x$ and it is shown in Fig. 14 at various times. We have chosen $\partial V_y/\partial x$ for the construction of PDF because $\partial V_y/\partial x$ is highly influenced by the presence of density stratification [21]. We have used 55 bins to construct the PDF. The skewness and kurtosis at time, $t = 50$, 100, 140, and 180 ω_{pd}^{-1} are (0.269595, 1.837707); (−0.108580, 1.782782); (−0.716172, 2.041251); and (−0.915989, 2.120084), respectively, as against a Gaussian whose skewness and kurtosis are (0, 0.25), (0, 0.36), (0, 0.40) and (0, 0.35) respectively. As the stratification in-

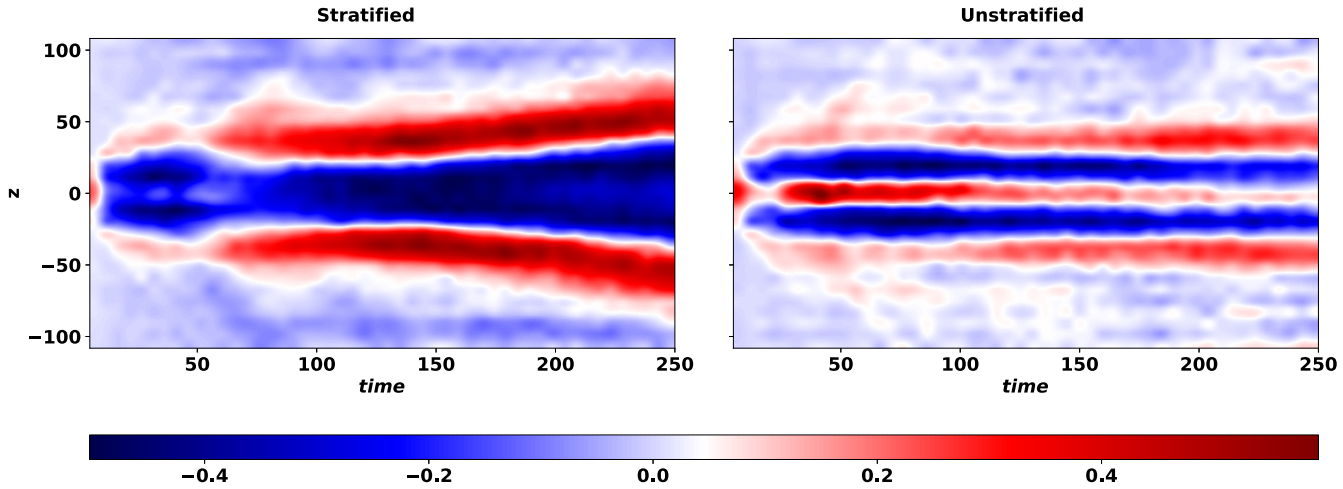

FIG. 12. Spatiotemporal plot for the stratified and unstratified case is shown. This diagram simply shows the spread of the turbulent spot and intermittency of the system. Increase in the length scale for the stratified case is evident from this diagram. Here, the zero velocity regions are considered as laminar while nonzero regions are considered as turbulent.

creases (as Froude number and Buoyancy Reynolds number decreases), the peak near zero of velocity gradient distribution increases due to increase in anisotropy or intermittency in the system (Ref. [21]). In our simulation as well, the height of the distributions near zero increase with time, which shows the presence of anisotropy or intermittency in the system. The height of the distributions at $t = 50$, 100, 140, and 180 ω_{pd}^{-1} are 59 613, 71 551, 86 818, and 102 348, respectively. As the height of the distributions increase with time, we normalize each distribution by its maximum height for the purpose of comparison (Fig. 14). Furthermore, the strong deviation of the probability distribution from the Gaussian also confirms the presence of intermittency or anisotropy present in the system.

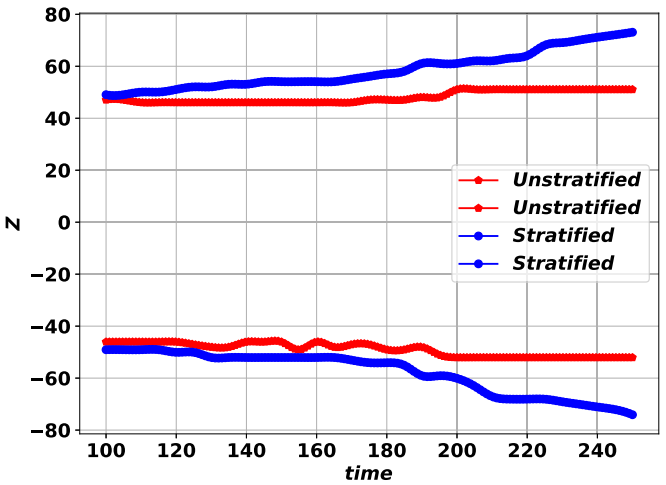

FIG. 13. The extent of the spot in the Z-t plane is shown. This diagram is plotted after tracking the edge of the spot, shown in Fig. 12. From this diagram, it is clear that the spread of the spot structure, along both side of Z is higher for the stratified case as compared to the unstratified case.

4. Streamwise vorticity

The velocity streak generation in a turbulent PCF primarily depends upon the streamwise vortices. The streaks are generated by the streamwise vortices through a lift-up mechanism, and the instability of streaks in turn re-energizes the streamwise vortices [50,51]. To calculate the streamwise vorticity, we have chosen the YZ plane at $X = 0$. In Fig. 15, we have shown the streamwise vortices for the stratified and unstratified cases. For the unstratified case, we observe well developed velocity streaks from $t = 40$–45 ω_{pd}^{-1} (Fig. 4) and at the same time two counter-rotating vortices also start to develop from $t = 45$ ω_{pd}^{-1} in Fig. 15. The two vortex structures are found to be symmetric about $\hat{z}$ direction. The vortex with positive vorticity is found to rotate clockwise and the other one with negative vorticity is found to rotate counter-clockwise. The vortex structures completely annihilate at around 165 ω_{pd}^{-1}. For the stratified case, the velocity streaks start to develop at around $t = 60$–65 ω_{pd}^{-1} and the two counter rotating vortices are also observed to develop from $t = 65$ ω_{pd}^{-1}. The vortex structures are observed to sustain for a longer period of time. The separation between the two vortices are found to increase with time and the symmetry of the two vortices along $\hat{z}$ direction is also observed for this case. It is to be noted that the velocity streaks for the unstratified case sustain (Fig. 4) even when the two oppositely signed streamwise vortex structures get destroyed beyond 150 ω_{pd}^{-1}, due to the presence of shear heating in the system [41]. It is well known that the velocity streaks are generated by streamwise vortices, and when the streaks split, it leads to the re-generation of streamwise vortices [50]. As for the unstratified case, there is no splitting of streaks observed earlier in the fluid velocity fields (Figs. 4 and 6), the feedback cycle from streaks to vortices and vice-versa may not be followed at late times. However, for stratified case, the cycle may be present, as vortices survive for longer duration (upto 250 ω_{pd}^{-1}) of time. It is interesting to see the vortices to survive for longer period of time for the stratified case, as compared to the unstratified case (shown in Fig. 15). Because, for both stratified and unstratified

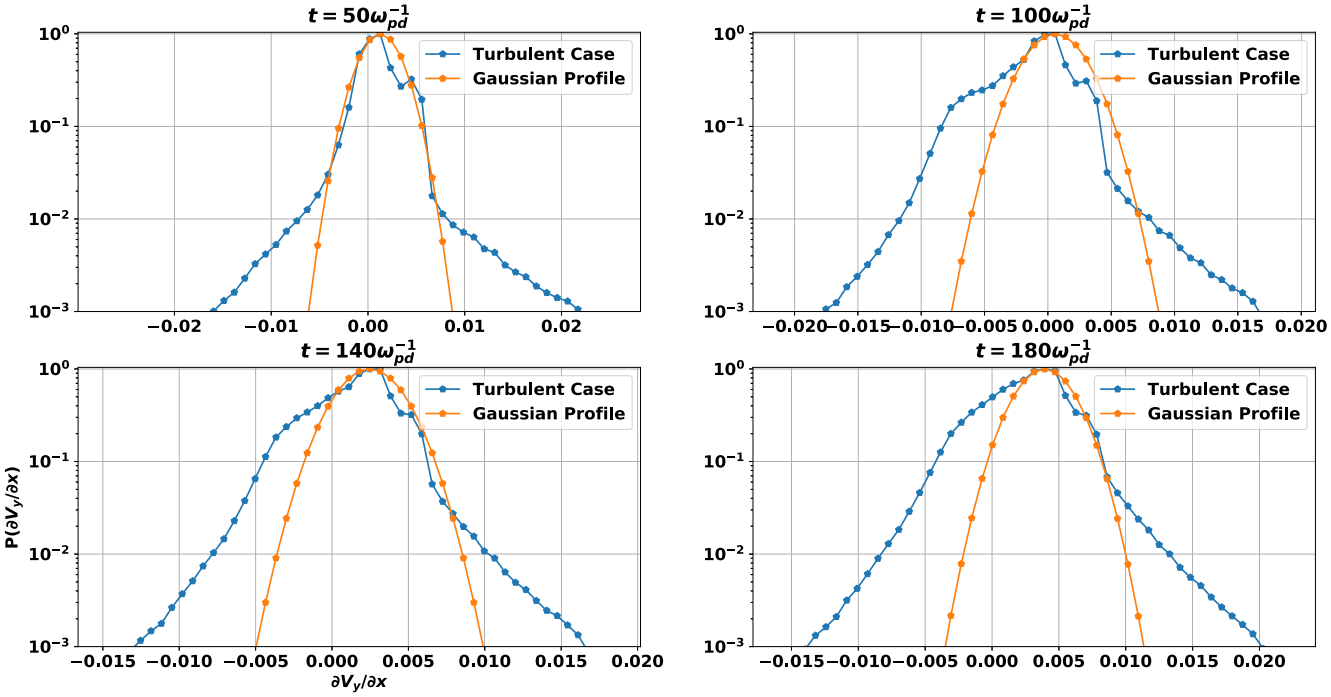

FIG. 14. The probability distribution function of $\partial V_y/\partial x$ for stably stratified turbulent (perturbed) case is shown in a log-linear plane. The number of bins considered to construct the distribution function is 55. Distribution strength below $1e-3$ are not shown. For the stably stratified turbulent cases, the Gaussian does not fit well. The height of the distribution is found to increase with time. The unnormalized height of the distributions at $t = 50$, 100, 140, and 180 ω_{pd}^{-1} are 59 613, 71 551, 86 818, and 102 348, respectively. In all the cases shown, the height of the distribution is normalized by the maximum height of each distribution.

cases, the initial perturbation strength is same (see Sec. II), the variation of Γ or the temperature is identical (Fig. 16) and the Reynolds number variation is also same for both the cases apart from a minute difference at the later times (Fig. 17) [30,52]. Despite having the parameters same for both the cases, the vortex structure for the stratified case survives for a longer period of time. Therefore, from the above results, we see that the ability of a stratified 3D Yukawa liquid to retain coherent structures for a longer period of time in a dissipative medium is remarkable and this needs further investigation.

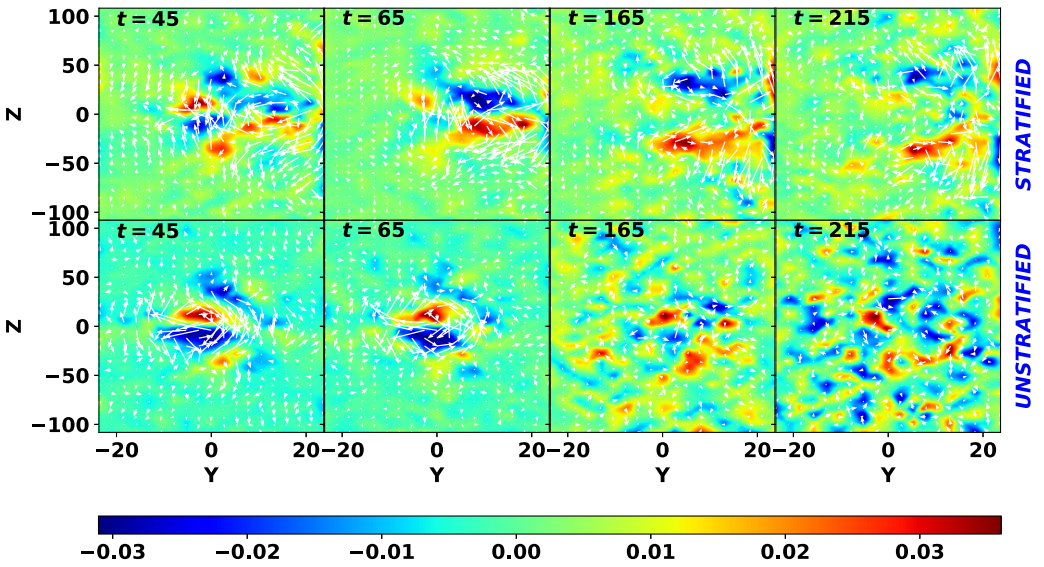

FIG. 15. The streamwise vortices for the stratified and unstratified cases at $X = 0$ as a function of YZ is shown. The streamwise counter-rotating vortices play an importaant role in the generation of the velocity streaks. The vortices survive for longer period of time for the stratified case and for the unstratified case, the structures are observed to diminish from 165 ω_{pd}^{-1}. Therefore, from the observation, one can surmise that a stratified 3D Yukawa liquid can preserve any coherent structure for a longer period of time as compared to that of a unstratified case.

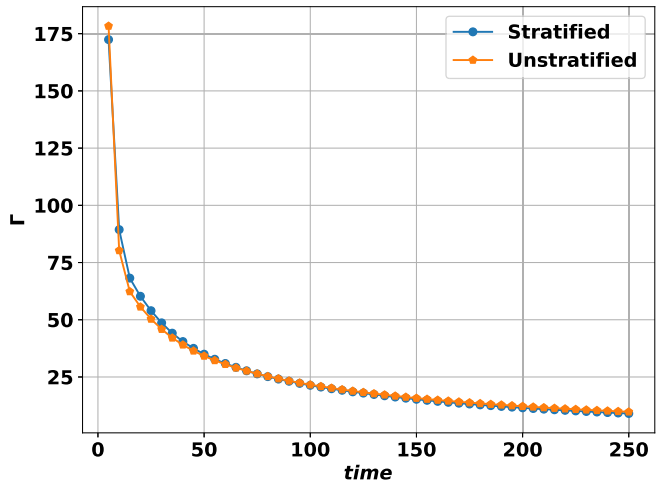

FIG. 16. Variation of Γ for the stratified and unstratified cases is shown. Despite the presence of an external gravity, Γ variation for the both the cases are same.

As we have already discussed about the upscale energy transfer and origin of velocity streaks, let us investigate the growth dynamics of the turbulent spot in terms of vertically averaged streamwise fluid velocity, which is also dubbed as "quadrupolar flow" diagnostics [37,53,54] in conventional hydrodynamics.

5. *Quadrupolar flow*

One of the important characteristics of a turbulent PCF in a 3D Yukawa liquid is that we observe Quadrupolar like flow around the turbulent spot at lower $\kappa(=1.0)$ value [30,37,53]. The flow is obtained and visualized by averaging the streamwise fluid velocity along the vertical direction ($\hat{y}$). The basic flow pattern is as follows: in the spanwise direction ($\hat{z}$), the flow is in the outward direction, and in the streamwise direction ($\hat{x}$), the flow is in the inward direction, as shown in Fig. 18. The quadrupolar flow starts to develop at 50 ω_{pd}^{-1}

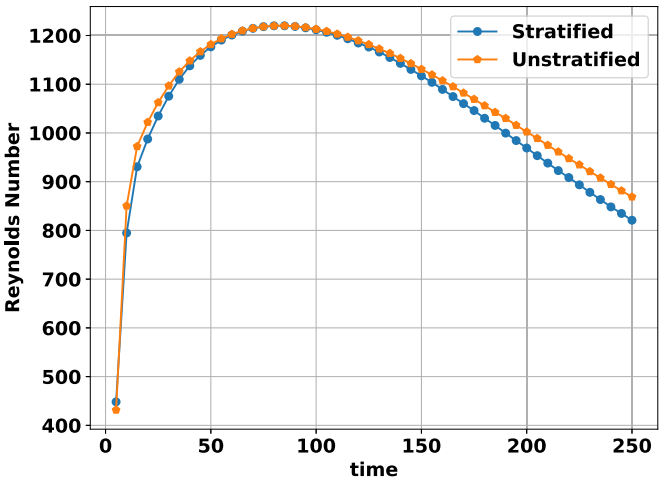

FIG. 17. Variation of Re with time for the two cases is shown. The time variation is the same for both cases, except there is a tiny variation after 150 ω_{pd}^{-1}.

for the unstratified case and becomes well-defined at around 100–110 ω_{pd}^{-1}. The quadrupolar flow has been observed to persist over time. For the stratified case, quadrupolar flow never observed to form. We observe a strong flow from positive $\hat{x}$ direction to negative $\hat{y}$ direction around $Y = 0$ from $t = 100$ to 200 ω_{pd}^{-1}. Moreover, the width of the central streak has increased with time. One of the main reasons for not observing the quadrupolar flow for the stratified case, is the presence of large-scale flow in the system. For the unstratified case, we observe a scale separation between relatively large and small wavelengths. However, such scale separation is not observed for the stratified case. It is because, the energy in the system is continuously storing in the larger wavelengths or larger scales.

B. Results for $\kappa = 4.0$

We have studied the system at $\kappa = 1.0$; we now study the system at $\kappa = 4.0$, in which the range of interaction is smaller as compared to the former cases. In our previous work [30], we have described that at higher range of interaction or at smaller κ values, our MD results tend to be more similar to the results obtained in conventional hydrodynamics. Here, we are considering a relatively higher value of κ (4.0), or smaller range of interaction. Consequently, the results for this case is unique and differs from that of the conventional hydrodynamics cases.

The spot formation process is studied at $\kappa = 4.0$, along with a weak external gravity ($g = 0.009 g_0$) applied to it. The total density variation for $\kappa = 4.0$ is shown in Fig. 2, after averaging over the vertically bounded $\hat{y}$ direction. The results for this particular case are presented below by comparing with the results obtained for the corresponding unstratified case.

1. V_x *fluid velocity*

The time evolution of the V_x fluid velocity field for the stratified case is shown in Fig. 19, along with the unstratified case, which is well known from our previous work [30]. For both the cases, we observe two velocity patches or the large scale structure or spot structure, one with positive velocity and the other with negative velocity. At the initial time, $t = 50$ ω_{pd}^{-1}, or before, the spot structure looks similar for both the cases. The structures are symmetric along $\hat{x}$ direction. At later times, $t = 150$ ω_{pd}^{-1}, the negative velocity patch is observed to shrink while the positive velocity patch is enlarged. For the unstratified case, the two velocity patches share almost the same area in the XZ plane. The symmetry along $\hat{x}$ direction of the overall spot structure is also broken. At around 175–180 ω_{pd}^{-1}, part of the negative velocity patch reappears on the right hand side of the simulation domain with a very small magnitude. On the other hand, the symmetry along $\hat{x}$ direction is still maintained for the unstratified case and the spot structure becomes more diffused. At around $t = 200$–210 ω_{pd}^{-1}, a portion of the negative velocity patch on the right hand side splits the positive part of the spot structure into two parts while for the unstratified case, the two velocity patches still survive and maintain the symmetry along $\hat{x}$ direction. It is well known from our previous work that the spot dynamics at $\kappa = 4.0$, is largely dominated by large-scale flow [30]. For the stratified case, the shrinking of the negative velocity patch of the spot structure at $t = 150$ ω_{pd}^{-1} and reappearance of the negative

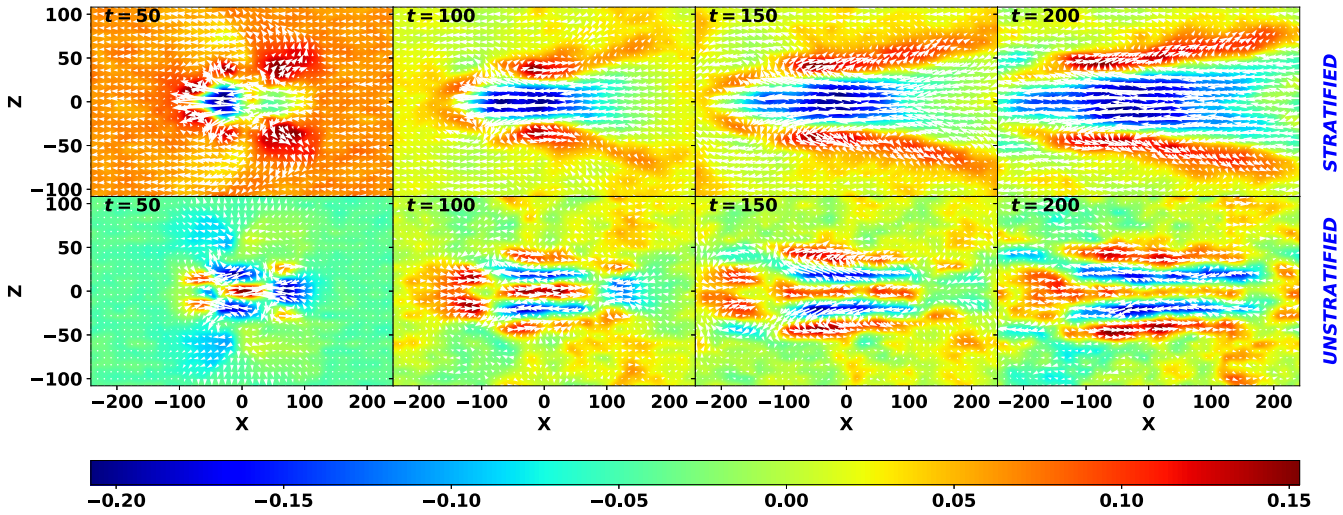

FIG. 18. Y averaged V_x fluid velocity field as a function of X and Z is shown. For the unstratified case, we observe the quadrupolar flow to form at $t = 50\ \omega_{pd}^{-1}$. For the stratified case, we do not observe the formation of quadrupolar flow and instead of that we observe a strong flow flowing from positive $\hat{x}$ to negative $\hat{x}$ direction at around $Z = 0$. We suspect that the absence of scale separation in the stratified case, is one of the main reasons for not forming the quadrupolar flow.

velocity patch on the right hand side of the simulation domain at $t = 175$–$180\ \omega_{pd}^{-1}$, may imply both decrease and increase of length scale of the system with time. This will be more clear when we perform Fourier analysis of the velocity data. As the large-scale structures persists through out the simulation time, a large-scale flow seems to be dominant for the stratified case. To know more about the dominant length scale or wave vector in the system, we perform Fourier analysis.

2. Analysis in Fourier space

We perform the 2D Fourier analysis (2D FFT) of the X kinetic energy, as we performed earlier. The instantaneous scale-weighted or premultiplied power spectra for the stratified and unstratified cases are shown in Fig. 20. To perform Fourier analysis, we follow the same procedure as we used for $\kappa = 1.0$. As the large-scale flow is dominant for this case, most of the energy is deposited in the higher wavelengths. Let us compare the scale-weighted energy ($K\hat{E}_x$) at the highest wavelength ($\lambda = 8.1648$) shown in Figs. 20(a) and 20(b). At the initial time ($t = 5\ \omega_{pd}^{-1}$), energy at larger wavelengths is very small and hence there is no large-scale flow present in the system. As the time evolves, large-scale flow start to develop in the system. From $t = 100$–$180\ \omega_{pd}^{-1}$, the energies are comparable. However, at $t = 100, 150\ \omega_{pd}^{-1}$, the energy for

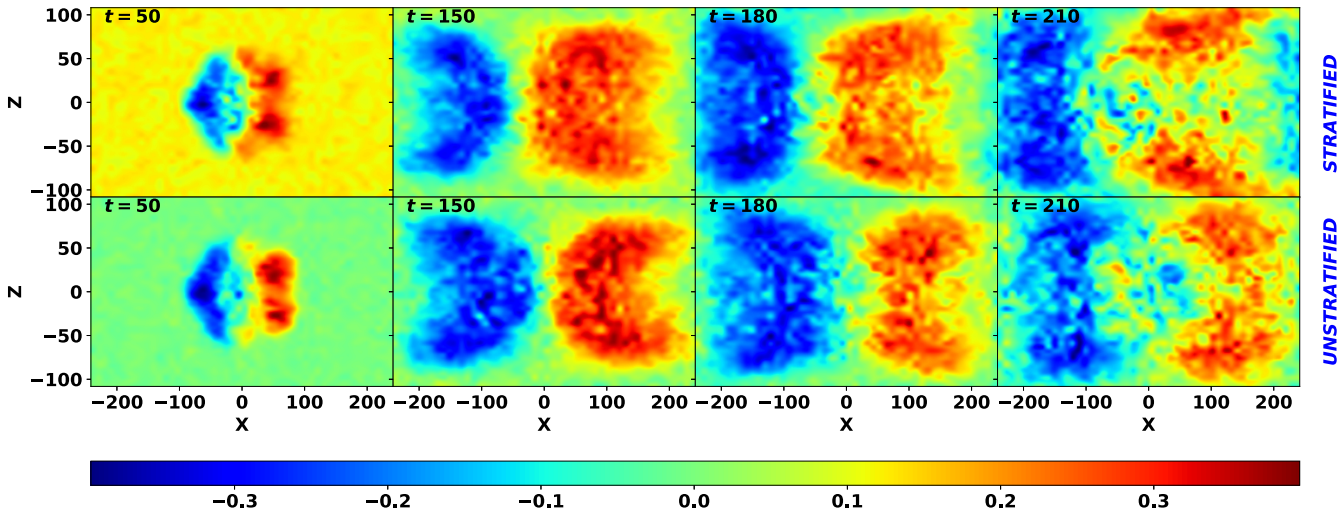

FIG. 19. Time variation of the spot structure in V_x fluid velocity field at $Y = 0$, as a function of X, Z for the stratified and unstratified cases is shown. For the unstratified case, the spot structure develops by maintaining the symmetry along $\hat{x}$ direction. At the initial time, the spot structures are almost identical, for both cases. For the stratified case, at $t = 150\ \omega_{pd}^{-1}$, the size of the two velocity patches vary. At $t = 180\ \omega_{pd}^{-1}$, a small part of the negative velocity patch re-appear on the right hand side of the domain. At $t = 210\ \omega_{pd}^{-1}$, the negative velocity patch on the right hand side breaks the positive part of the spot into two parts.

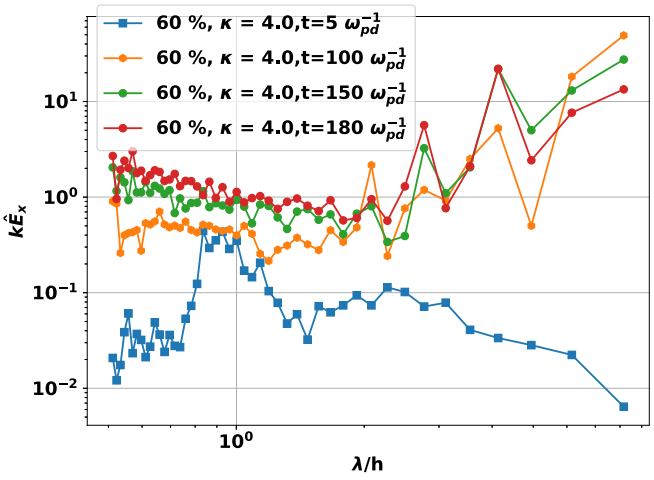

(a) Stratified case.

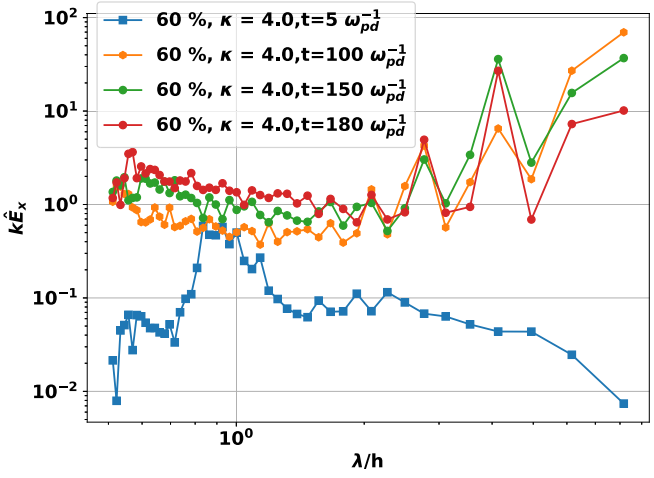

(b) Unstratified case.

FIG. 20. Instantaneous 2D scale-weighted or premultiplied power spectra for the stratified and unstratified case is shown. Both figures are in log-scale. As both the systems are dominated by large-scale flow, most of the energy is deposited in the highest wavelength($\lambda = 8.16h$). The energy at $\lambda = 8.16h$ is of the same order for both the cases, except few differences at the intermediate and late times. These few differences in the value of $K\hat{E}_x$ is playing a key role in governing the peculiar dynamics of the stratified system. (a) Stratified case. (b) Unstratified case.

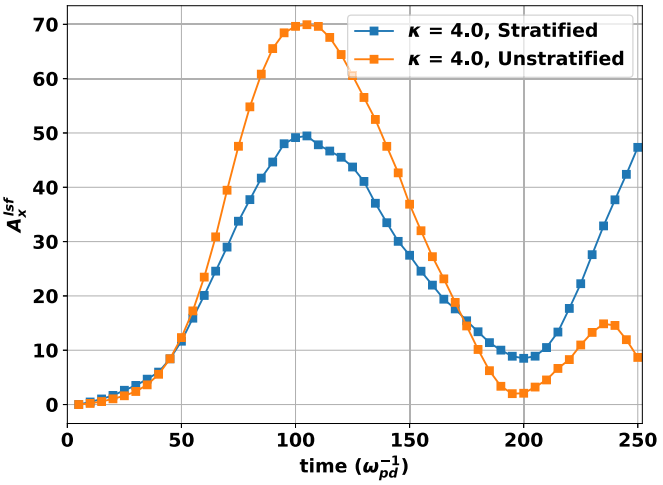

FIG. 21. Large-scale flow amplitude, A_x^{lsf} vs time for the stratified and unstraified cases is shown. The magnitude of A_x^{lsf} decreases for the stratified case at the intermediate time from around 70–160 ω_{pd}^{-1}. Beyond 170–175 ω_{pd}^{-1}, the magnitude of A_x^{lsf} is observed to increase. So, both decreasing and increasing behavior is observed for the stratified case, unlike the strongly growing nature, which is observed in Fig. 11(b), for $\kappa = 1.0$.

the unstratified case (69.62, 36.88) is higher than the stratified case (49.14, 27.48). However, at $t = 180\ \omega_{pd}^{-1}$, the energy for the stratified case (8.51) is higher as compared to the unstratified (2.08) one. Although, for both the cases the energy starts to decrease at the highest wavelength, the stratified case is observed to have smaller energy at the intermediate time ($t = 50$–$150\ \omega_{pd}^{-1}$), when the spot becomes well-defined; and higher energy at the late times ($t = 175\ \omega_{pd}^{-1}$ and more), as compared to the corresponding unstratified cases.

We perform the time averaging of the instantaneous scale-weighted spectra ($K\hat{E}_x$) to find the dominant wavelength (λ_m), in the same way as we performed earlier for $\kappa = 1.0$ case. We find λ_m to be 8.16 and the large-scale flow amplitude (A_x^{lsf}) for both the cases is shown in Fig. 21. The value of A_x^{lsf} is the same initially. At around $t = 55 - 60\ \omega_{pd}^{-1}$, the magnitude decreases for the stratified case. This might be due to the shrinking in size of the negative velocity patch as observed at $t = 150\ \omega_{pd}^{-1}$ in Fig. 19. Later, at $t = 175\ \omega_{pd}^{-1}$ and beyond, the magnitude of A_x^{lsf} for the stratified case increases. In the same time, part of the negative velocity patch re-appears on the right hand side of the simulation domain, as shown in Fig. 19 at $t = 180\ \omega_{pd}^{-1}$. Which implies that there is an increase in the length scale of the system. In other words, the external gravity refrains further decrease in the magnitude of A_x^{lsf}. From the above results we have observed that the magnitude of A_x^{lsf} decreases and increases with time under the influence of an applied external milligravity at $\kappa = 4.0$ or small interaction range.

After performing the Fourier analysis, we study the growth dynamics of the spot structure with the help of Y-averaged V_x velocity diagnostics

3. *Y-averaged streamwise fluid velocity*

The Y-averaged streamwise fluid velocity is shown in Fig. 22. At $t = 5\ \omega_{pd}^{-1}$, the spot structures look similar for both the cases. At $t = 50\ \omega_{pd}^{-1}$, a radially outward flow at zero velocity background is observed for the unstratified case. For the stratified case also, a radially outward flow is observed, but the flow along positive $\hat{x}$ direction becomes weak while the flow along negative $\hat{x}$ direction is much more stronger. At the same time, a flow from negative $\hat{x}$ direction to positive $\hat{x}$ direction is generated in the background for the stratified case. At $t = 100\ \omega_{pd}^{-1}$, a fully developed radially outward flow is observed for the unstratified case. For the stratified

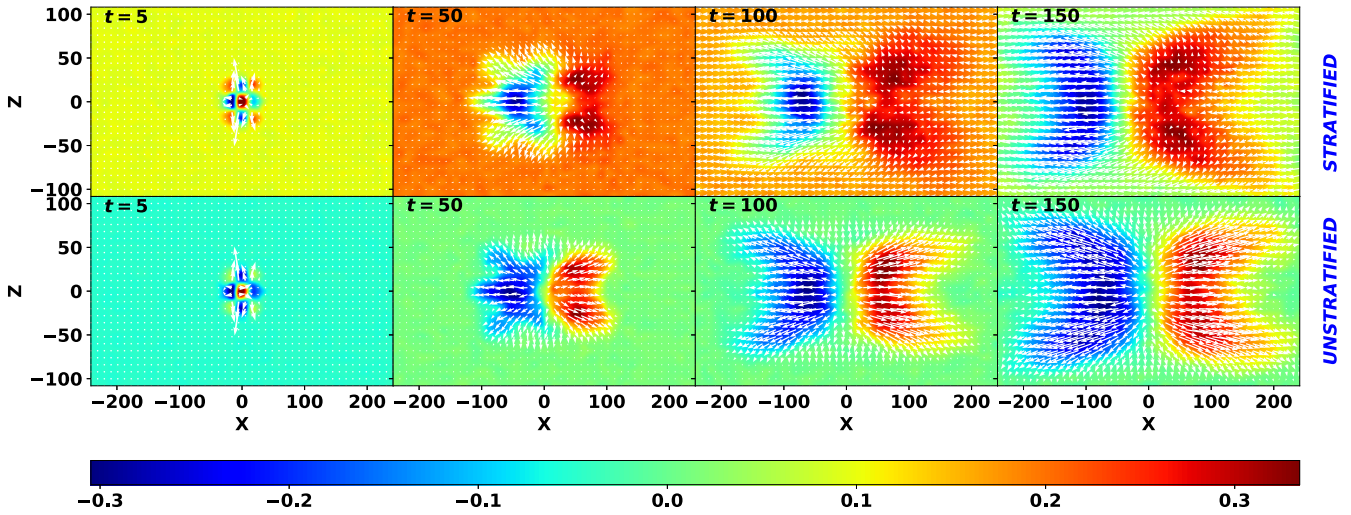

FIG. 22. Y averaged streamwise fluid velocity field for the stratified and unstratified case is shown. For the unstratified case, a uniform radially outward flow is observed in both parts of the spot in a zero velocity background. At $t = 5\ \omega_{pd}^{-1}$, the spot structure is nearly the same, except the magnitude, for both the cases. For the stratified case, at $t = 50\ \omega_{pd}^{-1}$, a background velocity is generated and observed to flow in negative $\hat{x}$ direction. The positive velocity patch becomes smaller than the negative one. At $t = 100\ \omega_{pd}^{-1}$, the background flow fully develops and tend to cover the entire XZ plane. The size of the positive velocity patch also becomes comparable with the negative one. At $t = 210$, the positive part of the spot structure becomes larger than the negative one and the entire spot structure observed to shift slightly towards negative $\hat{x}$ direction, which shows the increase in the length scale of the system due to the presence of the external milligravity. For the unstratified case, no background flow is generated and the spot structure evolves both symmetrically and equally with time.

case, a flow from negative $\hat{x}$ to positive $\hat{x}$ direction becomes fully developed in the background. The positive velocity patch hinder the background flow and only manages to change the flow direction a little bit. At $t = 150\ \omega_{pd}^{-1}$, the spot structure shifts towards left a little bit, breaking the symmetry along $\hat{x}$ direction for the stratified case. The positive velocity patch becomes larger in size as compared to the negative velocity patch. But the background velocity along negative $\hat{x}$ direction is so strong that the positive part of the spot structure only manages to change the direction of the background flow a little bit in the spanwise direction, which later takes the streamwise direction. For the unstratified case, the spot or velocity patches continue to grow symmetrically with strong radially outward flow and zero background velocity.

IV. CONCLUSION AND DISCUSSION

In this work, we have investigated the dynamics of a perturbed PCF in a stably stratified Yukawa liquid using 3D molecular-dynamics simulation. Upon applying a nonlinear 3D perturbations to the system, the system exhibits subcritical turbulence via spot formation. We have observed an upscale energy transfer or inverse cascading. The upscale energy transfer is first realized in fluid velocity diagnostics and then, it is verified by performing Fourier analysis. In fluid velocity fields V_x and V_y (Figs. 3–6), we find that both length and width of the spot structure has increased as compared to the unstratified case. Consequently, large-scale structure formation becomes evident. In Fourier space, we obtain results in support of the presence of large-scale structures in the system. From one dimensional Fourier transform analysis (Figs. 7 and 8), we observe that the energy continuously condenses at the smaller wave vectors ($K_x/K_{x_{\min}} \simeq 0$, $K_z/K_{z_{\min}} \simeq 2.0$), which implies that energy keeps on depositing at larger length scales. From two-dimensional Fourier transform analysis (Figs. 9 and 10), we observe that most of the energy has deposited in the higher wave-lengths (or lower wave vectors), confirming to the fact that the energy is continuously depositing at the highest length scale. Figure 11 shows the value of A_x^{lsf} for the stratified case is significantly higher as compared to the A_x^{lsf} for the unstratified case. Therefore large-scale flow appears to be more dominant in the stratified case as compared to the unstratified case.

Nucleation of a turbulent streak for $\kappa = 1.0$ in V_y fluid velocity fields is observed and it is shown in Fig. 5. It is a direct evidence of reinforcement of large-scale flow in the system. In conventional hydrodynamics, there are two known mechanisms, which are responsible for splitting and nucleation of new streaks [43,55]. The first mechanism is associated with the instability produced due to modified laminar flow or due to some stochastic behavior of the system, which leads to new streak generation. The second mechanism is associated with the growing spot, which is due to the presence of large-scale flow in the system. In our case, the second mechanism seems to be more probable, as due to the presence of external gravity, the magnitude of A_x^{lsf} has enhanced significantly (Fig. 11). It is also to be noted that the two mechanisms, which are mentioned above, is observed in a unstratified higher aspect ratio system ($A_x > 100$, $A_z > 50$) [43,55]. In addition to this, the Reynolds number of the above mentioned systems remain fixed with time. Hence, there is no dissipation due to viscosity, as we have in our case [30]. As a result of higher aspect ratios and fixed constant Reynolds number, the spot grows due to the

presence of the large-scale flow. The spot structure, which is a combination of large-scale flow + velocity streaks, grows in time and due to this growth, the streaks widen and finally split. In between the gap of the two split streaks, a new velocity streak is nucleated.

Coming back to our case, the aspect ratio is $A_x \simeq 10$. Moreover the Reynolds number decays with time in both cases—unstratified as well as stratified (see Fig. 17). Despite the presence of large-scale flow and growing turbulent spot, splitting and nucleation of streaks is not observed for the unstratified case [30]. However, as the magnitude of A_x^{lsf} enhances in the stratified case, splitting and nucleation of new streak is observed in Fig. 5. The splitting and generation of a new streak is a direct evidence of enhancement of large-scale flow or upscale energy transfer in the system. Such process involves "wavelength instability" [55], which we shall try to quantify more rigorously in our future work. However, we need to keep in mind that the large-scale flow in a system not only spreads the spot structure spatially but also suppresses the small scale structures. In Fig. 4, the reduction of velocity streaks from 5 to 3 for the stratified case is one example of it. In this case, there is a spanwise restriction in the generation of number of velocity streaks in V_x fluid velocity field. The same is expected for the V_y fluid velocity fields. However, it does not take place. At later times, the number of streaks become equal to that of the unstratified case (shown in Fig. 6). There seem to have a competition between the large and small scale flow in the system, which needs further investigation.

One more important property of a stratified Yukawa liquid, which is observed is that it can retain coherent structures for a longer period of time as compared to that of a unstratified case (Figs. 6, 15). The coherent structures in a dissipative system like Yukawa liquid, die out very quickly, because of the presence of shear heating in the system [30,56,57]. However, in the presence of an external gravity, the system retains the coherent structures for a longer period of time as compared to a unstratified case. Although, the Γ variation (Fig. 16) and Reynolds number (Fig. 17) variation with time is almost the same for both the cases. It is remarkable to observe such property of a stratified system in retaining coherent structures for a long period of time in a highly dissipative system like Yukawa liquid. However, life span of the coherent structures has enhanced, as result of increase in the length scale of the system. A further investigation of such property of a stratified Yukawa liquid will be performed in future.

The stratified dynamics is also studied at higher value of κ (4.0). We have observed from Figs. 19 and 21 that the presence of an external gravity reduces the large-scale flow at the intermediate times, but enhances at later times. For this case (at higher κ), the presence of an external gravity results in the decreasing and increasing behavior of large-scale flow in the system. Hence, the system behaves differently at different values of κ for the stratified case. The same phenomena was observed in our previous work [30] for a unstratified case. Such anomalous behavior at different κ will be investigated in future, more rigorously.

In Fig. 22, we have observed an unidirectional background flow from right to left for the stratified case for $\kappa = 4.0$. This indicates that there is an inhomogeneity in the base velocity profile (PCF), which may be introduced by the stable stratification present in the system. The inhomogeneity in velocity profile will be further investigated in future.

As we are using MD simulation to study hydrodynamic problems, it is natural to ask, is our simulation technique is better than DNS/LES? In MD, we have all the information at particle level and all the fluid variables are extracted from the instantaneous particle level information. Hence it is free from any "model" such as Navier-Stokes. The results obtained from MD simulations are thus based on "first principles" calculations.

We have discovered inverse cascade in a stably stratified PCF for the first time in a 3D Yukawa liquid. Experimental verification of some of the findings reported here—in both hydrodynamics and 3D Complex plasma system—will further strengthen these findings. For example, for experiments in hydrodynamics with stable stratification, one could use saline water to introduce stable stratification to the system. In a Complex plasma system, for both $\kappa = 1.0$ and 4.0, experiments could be performed in a parabolic flight, in which hypergravity and milligravity conditions become possible to execute [58].

ACKNOWLEDGMENT

All the work reported here has been performed in the 1 Petaflop Cluster "Antya", at the Institute for Plasma Research, Gandhinagar, India.

[1] R. H. Kraichnan, Kolmogorov's inertial-range theories, J. Fluid Mech. **62**, 305 (1974).
[2] A. Alexakis and L. Biferale, Cascades and transitions in turbulent flows, Phys. Rep. **767-769**, 1 (2018).
[3] R. H. Kraichnan, Inertial ranges in two-dimensional turbulence, Phys. Fluids **10**, 1417 (1967).
[4] Q. Chen, S. Chen, and G. L. Eyink, The joint cascade of energy and helicity in three-dimensional turbulence, Phys. Fluids **15**, 361 (2003).
[5] R. Marino, A. Pouquet, and D. Rosenberg, Resolving the paradox of oceanic large-scale balance and small-scale mixing, Phys. Rev. Lett. **114**, 114504 (2015).
[6] L. Biferale, S. Musacchio, and F. Toschi, Inverse energy cascade in three-dimensional isotropic turbulence, Phys. Rev. Lett. **108**, 164501 (2012).
[7] R. Young and P. L. Read, Forward and inverse kinetic energy cascades in jupiter's turbulent weather layer, Nat. Phys. **13**, 1135 (2017).
[8] L. Biferale, S. Musacchio, and F. Toschi, Split energy–helicity cascades in three-dimensional homogeneous and isotropic turbulence, J. Fluid Mech. **730**, 309 (2013).
[9] S. J. Benavides and A. Alexakis, Critical transitions in thin layer turbulence, J. Fluid Mech. **822**, 364 (2017).

[10] P. K. Yeung and Y. Zhou, Numerical study of rotating turbulence with external forcing, Phys. Fluids **10**, 2895 (1998).

[11] L. M. Smith and F. Waleffe, Transfer of energy to two-dimensional large scales in forced, rotating three-dimensional turbulence, Phys. Fluids **11**, 1608 (1999).

[12] C. Rorai, D. Rosenberg, A. Pouquet, and P. D. Mininni, Helicity dynamics in stratified turbulence in the absence of forcing, Phys. Rev. E **87**, 063007 (2013).

[13] D. Olvera and R. R. Kerswell, Exact coherent structures in stably stratified plane Couette flow, J. Fluid Mech. **826**, 583 (2017).

[14] D. A. Hebert and S. M. de Bruyn Kops, Predicting turbulence in flows with strong stable stratification, Phys. Fluids **18**, 066602 (2006).

[15] E. Lindborg, The energy cascade in a strongly stratified fluid, J. Fluid Mech. **550**, 207 (2006).

[16] G. Brethouwer, P. Billant, E. Lindborg, and J.-M. Chomaz, Scaling analysis and simulation of strongly stratified turbulent flows, J. Fluid Mech. **585**, 343 (2007).

[17] M. L. Waite, Stratified turbulence at the buoyancy scale, Phys. Fluids **23**, 066602 (2011).

[18] S. M. de Bruyn Kops and J. J. Riley, The effects of stable stratification on the decay of initially isotropic homogeneous turbulence, J. Fluid Mech. **860**, 787 (2019).

[19] P. Bartello and S. M. Tobias, Sensitivity of stratified turbulence to the buoyancy reynolds number, J. Fluid Mech. **725**, 1 (2013).

[20] S. Khani and M. L. Waite, Backscatter in stratified turbulence, Eur. J. Mech.: B/Fluids **60**, 1 (2016).

[21] S. M. de Bruyn Kops, Classical scaling and intermittency in strongly stratified Boussinesq turbulence, J. Fluid Mech. **775**, 436 (2015).

[22] S. Khani, Mixing efficiency in large-eddy simulations of stratified turbulence, J. Fluid Mech. **849**, 373 (2018).

[23] S. Khani and M. L. Waite, Effective eddy viscosity in stratified turbulence, J. Turbul. **14**, 49 (2013).

[24] R. Marino, P. D. Mininni, D. Rosenberg, and A. Pouquet, Inverse cascades in rotating stratified turbulence: Fast growth of large scales, Europhys. Lett. **102**, 44006 (2013).

[25] H. Charan and R. Ganesh, Observation of the Rayleigh-Bénard convection cells in strongly coupled Yukawa liquids, Phys. Plasmas **22**, 083702 (2015).

[26] P. Kaur and R. Ganesh, Negative entropy-production rate in Rayleigh-Bénard convection in two-dimensional Yukawa liquids, Phys. Rev. E **100**, 053201 (2019).

[27] P. Kaur and R. Ganesh, Phase of particle-level velocity perturbations determines the fate of Rayleigh–Bénard convection cells in 2D Yukawa liquids, Phys. Plasmas **28**, 063701 (2021).

[28] P. Kaur and R. Ganesh, Effect of particle mass inhomogeneity on the two-dimensional Rayleigh–Bénard system of Yukawa liquids: A molecular dynamics study, Phys. Plasmas **28**, 113703 (2021).

[29] J. Ashwin and R. Ganesh, Effect of external drive on strongly coupled Yukawa systems: A nonequilibrium molecular dynamics study, Phys. Rev. E **80**, 056408 (2009).

[30] S. Kalita and R. Ganesh, Spot formation in three-dimensional Yukawa liquid, Phys. Fluids **33**, 095118 (2021).

[31] P. K. Shukla and A. A. Mamun, *Introduction to Dusty Plasma Physics* (CRC Press, Boca Raton, FL, 2015).

[32] D. J. Evans, W. G. Hoover, B. H. Failor, B. Moran, and A. J. C. Ladd, Nonequilibrium molecular dynamics via gauss's principle of least constraint, Phys. Rev. A **28**, 1016 (1983).

[33] H. Charan, R. Ganesh, and A. Joy, Properties of gravitationally equilibrated Yukawa systems—a molecular dynamics study, Phys. Plasmas **21**, 043702 (2014).

[34] V. E. Fortov, A. V. Ivlev, S. A. Khrapak, A. G. Khrapak, and G. E. Morfill, Complex (dusty) plasmas: Current status, open issues, perspectives, Phys. Rep. **421**, 1 (2005).

[35] V. Nosenko and J. Goree, Shear flows and shear viscosity in a two-dimensional Yukawa system (dusty plasma), Phys. Rev. Lett. **93**, 155004 (2004).

[36] V. A. Romanov, Stability of plane-parallel Couette flow, Funct. Anal. Its Appl. **7**, 137 (1973).

[37] Y. Duguet and P. Schlatter, Oblique laminar-turbulent interfaces in plane shear flows, Phys. Rev. Lett. **110**, 034502 (2013).

[38] L. S. Tuckerman and D. Barkley, Patterns and dynamics in transitional plane Couette flow, Phys. Fluids **23**, 041301 (2011).

[39] A. Lundbladh and A. V. Johansson, Direct simulation of turbulent spots in plane Couette flow, J. Fluid Mech. **229**, 499 (1991).

[40] Y. Duguet, P. Schlatter, and D. S. Henningson, Formation of turbulent patterns near the onset of transition in plane Couette flow, J. Fluid Mech. **650**, 119 (2010).

[41] A. Gupta, R. Ganesh, and A. Joy, Molecular shear heating and vortex dynamics in thermostatted two dimensional Yukawa liquids, Phys. Plasmas **23**, 073706 (2016).

[42] F. Daviaud, J. Hegseth, and P. Bergé, Subcritical transition to turbulence in plane Couette flow, Phys. Rev. Lett. **69**, 2511 (1992).

[43] M. Couliou and R. Monchaux, Growth dynamics of turbulent spots in plane Couette flow, J. Fluid Mech. **819**, 1 (2017).

[44] P. Manneville, On the decay of turbulence in plane Couette flow, Fluid Dyn. Res. **43**, 065501 (2011).

[45] A. Prigent and O. Dauchot, Transition to versus from turbulence in subcritical Couette flows, in *IUTAM Symposium on Laminar-Turbulent Transition and Finite Amplitude Solutions* (Springer, Berlin, 2005), pp. 195–219.

[46] J. Philip and P. Manneville, From temporal to spatiotemporal dynamics in transitional plane Couette flow, Phys. Rev. E **83**, 036308 (2011).

[47] M. Couliou and R. Monchaux, Childhood of turbulent spots in a shear flow, Phys. Rev. Fluids **3**, 123901 (2018).

[48] G. Brethouwer, Y. Duguet, and P. Schlatter, Turbulent–laminar coexistence in wall flows with coriolis, buoyancy or lorentz forces, J. Fluid Mech. **704**, 137 (2012).

[49] M. Couliou and R. Monchaux, Large-scale flows in transitional plane Couette flow: A key ingredient of the spot growth mechanism, Phys. Fluids **27**, 034101 (2015).

[50] J. M. Hamilton, J. Kim, and F. Waleffe, Regeneration mechanisms of near-wall turbulence structures, J. Fluid Mech. **287**, 317 (1995).

[51] F. Waleffe, On a self-sustaining process in shear flows, Phys. Fluids **9**, 883 (1997).

[52] S. Khrapak, Practical formula for the shear viscosity of Yukawa fluids, AIP Adv. **8**, 105226 (2018).

[53] J. Schumacher and B. Eckhardt, Evolution of turbulent spots in a parallel shear flow, Phys. Rev. E **63**, 046307 (2001).

[54] Z. Wang, C. Guet, R. Monchaux, Y. Duguet, and B. Eckhardt, Quadrupolar flows around spots in internal shear flows, J. Fluid Mech. **892**, A27 (2020).

[55] M. Couliou and R. Monchaux, Spreading of turbulence in plane Couette flow, Phys. Rev. E **93**, 013108 (2016).

[56] A. Gupta, R. Ganesh, and A. Joy, Kolmogorov flow in two dimensional strongly coupled Yukawa liquid: A molecular dynamics study, Phys. Plasmas **22**, 103706 (2015).

[57] J. Ashwin and R. Ganesh, Kelvin Helmholtz instability in strongly coupled Yukawa liquids, Phys. Rev. Lett. **104**, 215003 (2010).

[58] A. Seidel, W. Soellner, and C. Stenzel, EML–An electromagnetic levitator for the international space station, J. Phys.: Conf. Ser. **327**, 012057 (2011).